Numerical Simulation Analysis of Influence of Wind and Temperature on Deformation of Constructed Zhaidi River High Bridge Pier

Mengnan Tian[1], Jinzhong Sun[1,*], Xiang Chen[2] and Feng Xiong[3]

[1] School of Engineering and Technology, China University of Geosciences, Beijing, 100083, China

[2] School of Civil Engineering, Beijing Jiaotong University, Beijing, 100044, China

[3] School of Civil Engineering, Hefei University of Technology, Hefei, 230009, China

Revista Internacional
Métodos numéricos
para cálculo y diseño en ingeniería
RIMNI
UNIVERSITAT POLITÈCNICA DE CATALUNYA BARCELONATECH
In cooperation with CIMNE

INFORMATION

Keywords:
High bridge pier
wind-induced deformation
temperature-induced deformation
solar radiation
air temperature variation
numerical simulation

DOI: 10.23967/j.rimni.2025.10.66560

SCIPEDIA Revista Internacional de Métodos Numéricos para Cálculo y Diseño en Ingeniería

Revista Internacional Métodos numéricos para cálculo y diseño en ingeniería RIMNI

In cooperation with CIMNE

Numerical Simulation Analysis of Influence of Wind and Temperature on Deformation of Constructed Zhaidi River High Bridge Pier

Mengnan Tian[1], Jinzhong Sun[1,*], Xiang Chen[2] and Feng Xiong[3]

[1]School of Engineering and Technology, China University of Geosciences, Beijing, 100083, China

[2]School of Civil Engineering, Beijing Jiaotong University, Beijing, 100044, China

[3]School of Civil Engineering, Hefei University of Technology, Hefei, 230009, China

ABSTRACT

Bridges are key projects of high-grade Expressways in mountainous areas. The verticality of bridge piers with a height of more than 100 m is crucial to ensure the safety and stability of bridge projects. When a pier construction is completed but the upper beam structure has not yet been connected (so-called after construction or constructed), the verticality of the pier is most likely to vary due to some factors. Based on the Zhaidi River Bridge project of Yunnan Zhenhe Expressway, considering the natural environment of the bridge site, three wind force intensity levels (Beaufort Scale 8, 10, and 12) and two climate conditions (high temperature and high radiation in summer, and low temperature and low radiation in winter) were identified; and the wind-induced deformation, temperature-induced deformation, and wind-temperature coupled deformation of the constructed main pier of the Zhaidi River Bridge with a height of 112.60 m were simulated with ANSYS Workbench numerical simulation platform. The simulation results show that: the influence of wind on pier deformation is much greater than that of ambient temperature variation; the influence of solar radiation on temperature-induced deformation of the bridge pier is much greater than that of air temperature variation; the temperature-induced deformation of the pier body under low temperature and low radiation condition in winter is greater than that under high temperature and high radiation condition in summer; the directional effect of the superposition of wind-induced deformation and temperature-induced deformation is more significant under low temperature and low radiation condition in winter.

OPEN ACCESS

Received: 11/04/2025

Accepted: 16/10/2025

Published: 23/01/2026

DOI
10.23967/j.rimni.2025.10.66560

Keywords:
High bridge pier
wind-induced deformation
temperature-induced deformation
solar radiation
air temperature variation
numerical simulation

1 Introduction

In mountainous areas, the construction of high-grade highways and railways often requires numerous bridges. Some bridge piers may reach heights exceeding 100 m, commonly referred to as "high bridge pier". It is evident that the verticality of the bridge piers, especially for those that are

*Correspondence: Jinzhong Sun (sunjinzhong@foxmail.com).

very tall, plays a crucial role in the overall stability of the bridge. When a bridge pier is completed but the upper beam structure has yet to be connected (so-called "after construction state" or "constructed pier"), the verticality of the bridge pier is most susceptible to various factors. The variation in the verticality of the bridge pier comes from the deformation of the pier body. The significance of the analysis of the deformation of a high bridge pier after construction is to fully consider the potential impacts of various possible factors on the deformation and stability of the bridge pier, and provide substantial and concrete evidence for the design and quality control of high bridge piers.

The factors that lead to the verticality variation of constructed bridge piers can be categorized into two types: inherent defects and external conditions. Inherent defects can be eliminated by strictly controlling the construction quality, making them controllable factors. External conditions, primarily natural environmental factors such as wind force (wind load) and temperature variation (temperature load), are highly random. Wind force and temperature variation can cause uneven deformation at different heights of a bridge pier, leading to significant variations in the verticality of high bridge piers. Fully considering the impacts of wind force and temperature variation on the verticality of constructed high bridge piers is of great importance for bridge design and construction.

Although the significant impact of wind forces on bridge safety has long been recognized [1], and extensive studies have been conducted on the effects of wind loads on bridge deformation, research focusing on the deformation of ultra-high bridge piers under wind action remains relatively limited. Existing studies have demonstrated significant wind load effects on ultra-high bridge piers. Tvrda [2] introduces a computational method using direct numerical integration and Gaussian/Newton-Cotes cubic, highlighting deviations from classical elasticity theory in the calculation of high bridge piers. Han et al. [3] employed finite element analysis and random vibration theory to investigate the wind effects on rigid-frame bridges with twin-legged high piers during the erection phase. Their study accounted for various wind load components, buffeting forces, and aerodynamic admittance functions. Further investigations by Wu et al. [4] calculated the wind loads on long-span high-pier box-girder bridges according to different national codes. Their calculation results showed that wind loads increase with both elevation above the ground and the height of the bridge pier. Computational fluid dynamics (CFD) is widely used in simulations and wind tunnel experiments of the dynamic response of slender, tall bridge piers to wind loads [5]. These methods help to understand the complex interactions between wind and structural components, such as bridge piers and decks.

Through numerical analysis, Dai et al. [6] found that the temperature variation from the sun-exposed side to the shaded side in the cross-section of a high bridge pier follows a negative exponential function, and the depth of sunlight temperature influence is about 0.60 m. Chen et al. [7] developed a model to predict average temperature variations in hollow concrete piers based on long-term observations, which enhanced understanding of thermal uniformity and supporting strategies to mitigate thermal effects in bridge design. Through finite element analysis, Li et al. [8] revealed that thermal stress and deformation caused by temperature differences and cold waves concentrate at the bridge pier corners, so they suggested that rounded chamfers should be added to reduce stress concentration. An et al. [9] derived a formula for calculating the temperature deformation of the line shape of a thin-walled hollow pier body using an analytical algorithm, which can more accurately account for sunlight temperature differences and pier height. Studies [10,11] indicated that thermal cracking due to concrete hydration heat, though not caused by natural temperature-induced deformation, demonstrates that non-uniform temperature field distribution significantly impacts the structural integrity of high bridge piers.

Recent years, the effects of wind loads or temperature loads on the structural performance, stability and deformation of high bridge piers have been explored respectively; additionally, the impacts of other types of loads (such as seismic load, tidal load, etc.) on bridge structures have also been studied [12–16]. However, there are very few reports on the effects of the superposition and coupling of wind action and temperature variation on the deformation of thin-walled high bridge piers.

From the perspective of research methods, the contour and cross-sectional shape of high bridge piers are often complex, making it difficult to derive analytical solutions for the effects of temperature variations and wind forces on the deformation of high bridge piers. As a result, numerical simulation is currently the primary research method for the deformation problems of high bridge piers.

To address these research gaps mentioned above, this paper takes the high bridge pier of the Zhaidi River Bridge in the mountainous region of southwest China as a case, and employs ANSYS Workbench for detailed numerical simulations, which is consistent with the current trend of the analytical method applied in the field of bridge engineering [17], to conduct a systematic study on the effects of wind action, temperature variation, and the superposition coupling of the two on the deformation of thin-walled concrete bridge piers, in order to provide a scientific basis for considering the superposition and coupling effects of wind action and temperature variation in the design and construction of high bridge piers in complex mountainous environments. These studies fill the gap in the superposition coupling effect analysis of wind action and temperature variation on the deformation of high bridge pier after construction, and have significant theoretical and engineering value.

2 Overview of the Zhaidi River Bridge Project

The Zhaidi River Bridge serves as a critical infrastructure of the Zhen-He Expressway crossing the Zhaidi River. The Zhen-He (Zhenxiong-Hezhang) Expressway, an important section of the inter-provincial expressway "Yibin-Liupanshui Expressway", is in Zhenxiong County, Zhaotong City, Yunnan Province, close to the provincial border of Yunnan and Guizhou. The expressway section where the Zhaidi River Bridge is located is built to the standard of a two-way, four-lane expressway with an integral roadbed width of 25.5 m. Fig. 1 shows the Zhaidi River Bridge on the Zhen-He Expressway under construction.

2.1 Natural Environment and Engineering Geology Conditions of the Bridge Site

2.1.1 Geographical Location and Topography

The bridge site is in Zhongtun Town, Zhenxiong County, which lies in the middle mountain slope zone in the northern part of the Yunnan-Guizhou Plateau and belongs to a tectonic and erosional low-middle mountain landform area with undulating mountains and crisscrossing gullies. The river width at the intersection of the Zhaidi River and the Expressway is about 2.5 m, with a water depth of 0.5 to 2.0 m, which is mainly replenished by atmospheric precipitation and gullies and streams along the route. The bridge is designed to span the Zhaidi River, and the ground elevation along the centerline of the bridge site ranges from approximately 1410 m to 1560 m, with a maximum relative height difference of 150 m. The Zhaidi River Valley, where the bridge crosses, runs in the direction of NNW direction (approximately 350°, roughly corresponding to the valley' s wind direction), while the axis of the bridge is in the direction of about 240°.

Figure 1: The Zhaidi River Bridge under construction on the Zhenhe Expressway (viewed northward)

2.1.2 Meteorological, Hydrological, and Geological Conditions

The Zhaidi River Bridge project area has a warm temperate monsoon climate, and some river valley areas have a subtropical climate, with an annual average temperature is 11.3°C, 1341 h of sunshine, 218.6 days of frost-free period, and an annual average precipitation of 914.6 mm.

The overburden of the bridge site is mainly Quaternary (Q_{4al}) silty clay and slope accumulation (Q_{pdl}) silty clay. The exposed bedrock is the Maokou Formation (P_{1m}) limestone of the Lower Permian System, including thin-thick layered strongly weathered limestone with a thickness of about 1.7 m (basic allowable value of bearing capacity $[f_{a0}] = 500$ kPa, standard value of friction resistance $q_{ik} = 120$ kPa) and underlying extremely thick medium-thick layered moderately weathered limestone (basic allowable value of bearing capacity $[f_{a0}] = 1500$ kPa, standard value of friction resistance $q_{ik} = 300$ kPa).

2.2 Key Design Technical Specifications and Pier Structure of the Zhaidi River Bridge

2.2.1 Technical Specifications

As shown in Fig. 2, the starting mileage pile number of the Zhaidi River Bridge is K8+517, and the ending mileage pile number is K8+863. The starting point is on the Zhenxiong side, and the end point is on the Hezhang side. The total length of the bridge is 346 m. The main design technical specifications of the bridge are as follows [18]:

(1) Traffic Speed—80 km/h; (2) Vehicle Load—Highway Class I; (3) Bridge Width—25.5 m; (4) Design Flood Frequency—1/100 (1 in 100 years); (5) Seismic Parameters—According to the China Earthquake Ground Motion Parameter Zonation Map (GB 18306-2015) [19], the peak ground acceleration is 0.05 g, the characteristic period of the seismic response spectrum is 0.4 s, the basic seismic intensity is VI, and the fortification intensity is VII; (6) Environmental Category—Class I; (7) Wind Load—Calculated according to Article 4.3.7 of the "General Specifications for Design of Highway Bridges and Culverts" (JTG D60-2004) [20], with key parameters $k_0 = 1.0$, $k_3 = 1.4$, $k_5 = 1.7$,

and a basic design wind speed of 28.2 m/s; (8) Temperature Load—The overall temperature both in the longitudinal and transverse directions of the bridge rises and falls evenly by ±14°C.

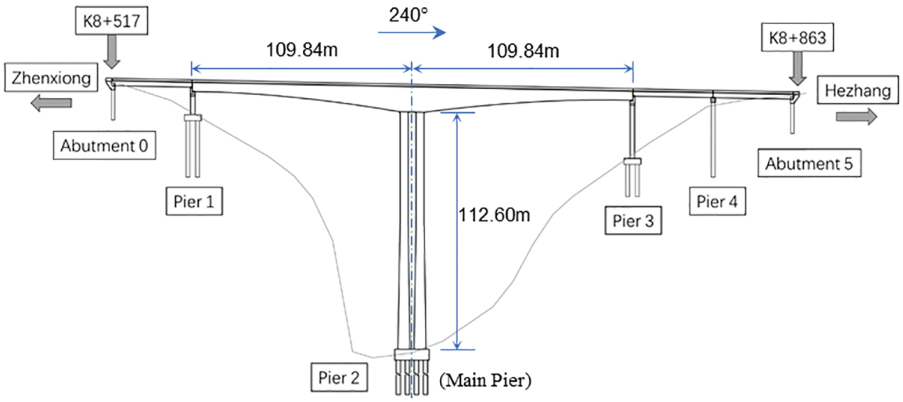

Figure 2: Schematic elevation of the Zhaidi River Bridge (viewed southward)

2.2.2 Pier Structure

As shown in Fig. 2, there are four piers in the middle and one abutment at each end of the Zhaidi River Bridge. The piers and the abutments are numbered uniformly: 0# (starting abutment), 1#∼4# (piers), and 5# (terminal abutment) from the starting point to the ending point of the bridge. Among them, Pier 2# with a height of 112.60 m is set at the deepest part of the river valley and serves as the main pier of the Zhaidi River Bridge. The pier 2# (the main pier) of the Zhaidi River Bridge is the research object of this paper for high bridge pier deformation. The specific description of the structure of the pier 2# is as follows:

(1) The main pier under the superstructure of the bridge consists of the pier, bearing abutment (pile cap), and pile foundation from top to bottom. The superstructure is made of C55 concrete, the bearing cushion stone of the abutment is made of C30 concrete, the pier and pile cap are constructed using C40 concrete, and the pile foundation material is C30 underwater concrete. Technical standards of the concrete comply with the provisions of GB 50010-2010 (2015 version) "Code for Design of Concrete Structures" [21], JTG 3362-2018 "Specifications for Design of Highway Reinforced Concrete and Prestressed Concrete Bridges and Culverts" [22], JTG/T 3650-2020 "Technical Specifications for Construction of Highway Bridges and Culverts" [23], and GBT 50476-2019 "Standard for Durability Design of Concrete Structures" [24].

(2) The main pier (Pier 2#) of the bridge is in the center of the Zhaidi River valley. It is a variable-section reinforced concrete rectangular thin-walled double-limb hollow pier. There are 2 sub-piers on each side of the two-way (connected by a short crossbeam in the middle), totaling 4 sub-piers. The cross-section of the pier bottom layout on the pier base table is shown in Fig. 3, and the overall structure of the pier is shown in Fig. 4. The cross-sectional dimension on the bottom of each sub-pier is 10 m × 6 m (transverse × longitudinal), and the cross-sectional dimension on the top of the sub-pier is 6.5 m × 4.0 m (transverse × longitudinal), where the transverse direction is perpendicular to the axis of the bridge, and the longitudinal direction is along the axis of the bridge. The cross-section of the pier body variable from the pier bottom to the height of 62 m, and constant from the height of 62 m to the pier top. The main pier sits on the bearing abutment (pile cap) with dimensions (length × width × height) of 2610 mm ×

1710 mm × 550 mm, which is supported by a pile foundation consisting of 24 Φ2.2 m bored concrete-cast piles embedded in rock mass. The height of the main pier above the pile cap is 112.60 m.

(3) Each pier is designed as a flexible pier. The horizontal force is distributed according to the integrated stiffness distribution method. The reinforcement design is carried out according to the ultimate bearing capacity state based on the internal force of the controlled section, and the structural crack width is controlled according to the normal serviceability limit state.

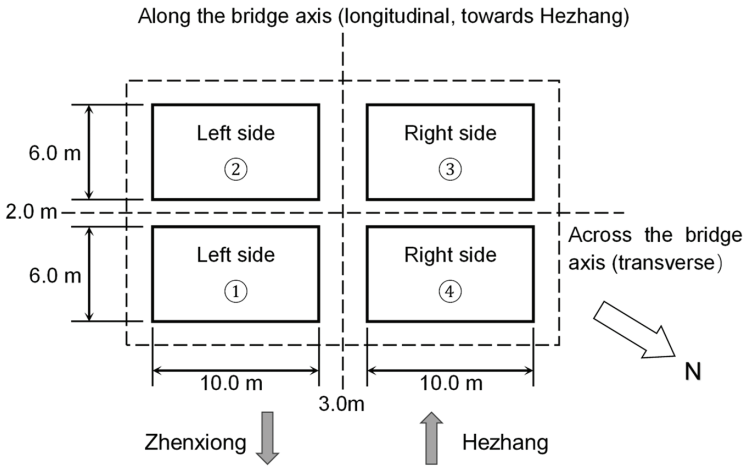

Figure 3: Cross-section of the pier bottom layout on the pier base table of Pier 2# (main pier) of the Zhaidi River Bridge (left side is the lane to Zhenxiong direction and right side is the lane to Hezhang direction)

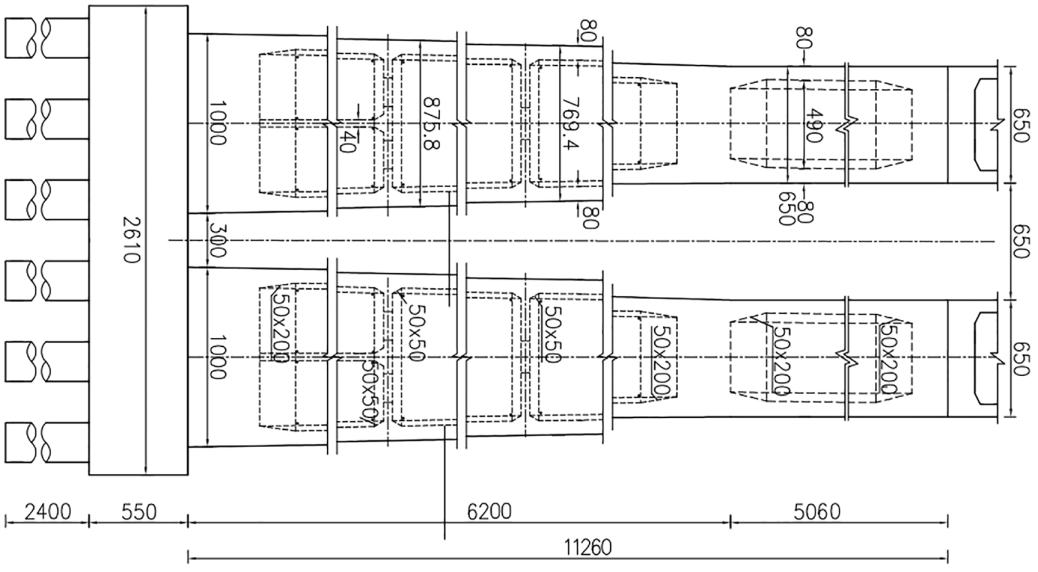

Figure 4: (Continued)

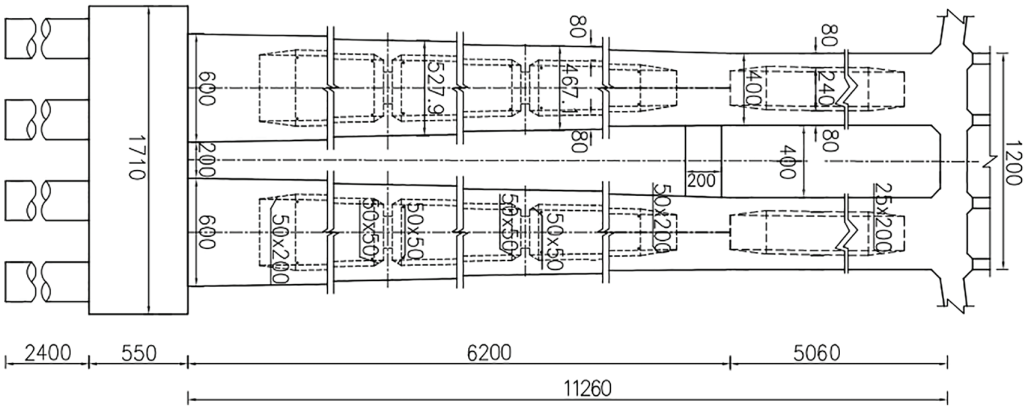

Figure 4: Structural diagram of Pier 2# (main pier) of the Zhaidi River Bridge. (Sizes noted unit in the figure is cm)

3 Numerical Model of Wind-Induced Deformation and Temperature-Induced Deformation of the Zhaidi River Bridge High Pier

Given the natural environment and engineering characteristics of the Zhaidi River Bridge, wind force and temperature variation are the two primary natural loads affecting the deformation of the piers after construction. According to the design scheme of the Zhaidi River Bridge, a numerical model for the main pier of the Zhaidi River Bridge is established. In consideration of the wind force characteristics influenced by the local topography and landform constraints, and the sunshine conditions and weather conditions corresponding to the geographical latitude, the thermal-mechanical coupling analysis method of ANSYS finite element was used to numerically simulate the deformation of the constructed high pier caused by wind force and temperature variation. Through simulation analysis, this study attempts to reveal the influence patterns and extent of wind force and thermal variation on the deformation of constructed bridge piers. The study findings serve dual purposes: (1) verify the rationality of the bridge pier design, and (2) provide robust technical evidence for the formulation of engineering countermeasures to ensure the verticality and safety of the Zhaidi River high bridge pier.

3.1 Numerical Modeling of Bridge Piers

3.1.1 Numerical Simulation Model and Observation Coordinate System of Bridge Pier

Numerical Simulation Model of Bridge Pier

The ANSYS numerical simulation model of the main pier of the Zhaidi River Bridge was constructed at a 1:1 scale, strictly adhering to the construction drawings (Fig. 4). The rendered model is illustrated in Fig. 5.

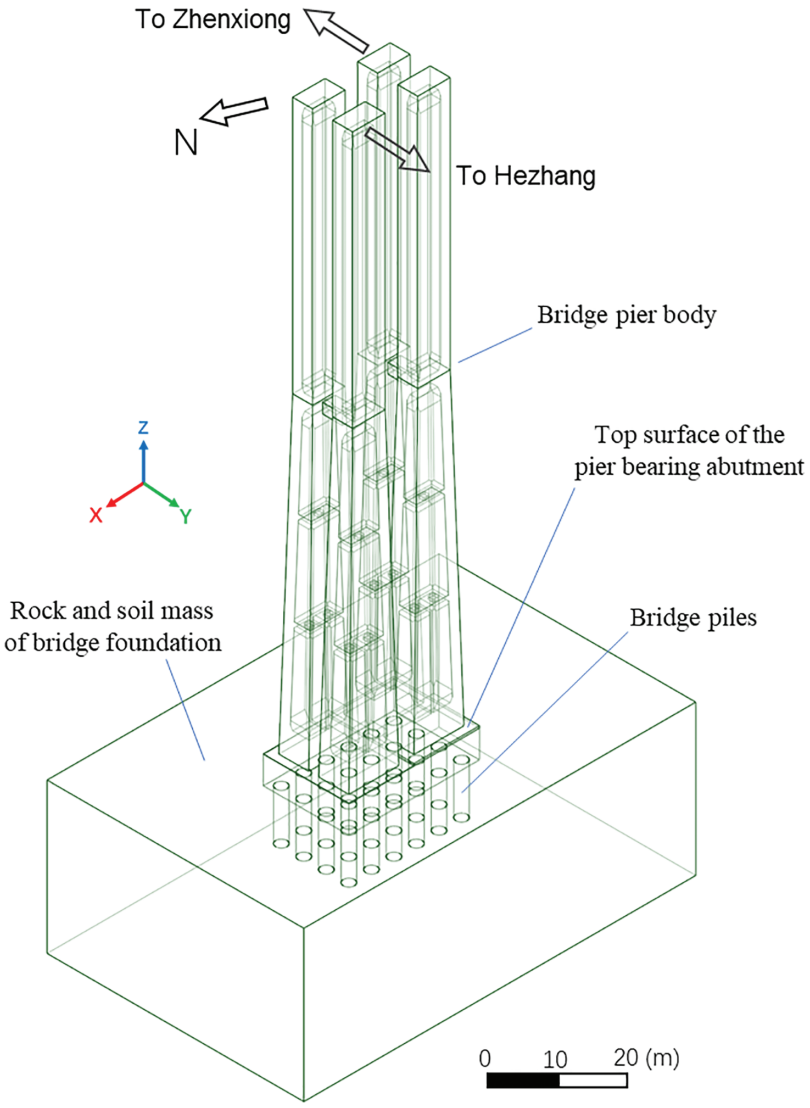

Figure 5: ANSYS numerical simulation model rendering of the intact main pier of the Zhaidi River Bridge

Local Coordinate System of Bridge Pier

To facilitate analysis and discussion, it is necessary to define the naming conventions and local observation coordinate systems of the bridge piers. As shown in Fig. 6, the two sub-piers heading towards Zhenxiong (left lane of the Expressway) are numbered as ① and ②, while the two sub-piers heading towards Hezhang (right lane of the Expressway) are numbered as ③ and ④. The local coordinate system (X, Y, Z) adopted for modeling establishes the X-Y plane as horizontal. The Y-axis is parallel to the axis of the bridge (the Expressway) and points to the direction of increasing highway mileage (towards Hezhang), that is, the positive direction of the Y-axis points to 240°. The X-axis is perpendicular to the bridge axis (along the valley direction), and its positive direction points to 330°, deviating by 20° from the valley orientation of 350°. The Z-axis is directed vertically upward, completing a right-handed coordinate system. As shown in Fig. 6, the origin of the coordinate system

(X, Y, Z) is located at the east corner point on the top surface of the pier base table near the pier ①. The four side surfaces of each sub-pier are named according to their external normal direction relative to the coordinate system. As shown by the notations on Sub-Pier ② in Fig. 6, the four side surfaces of Sub-Pier ② are named X, $-X$, Y, and $-Y$, respectively. The naming convention for the side surfaces of other Sub-Piers follows the same rules as for Sub-Pier ②.

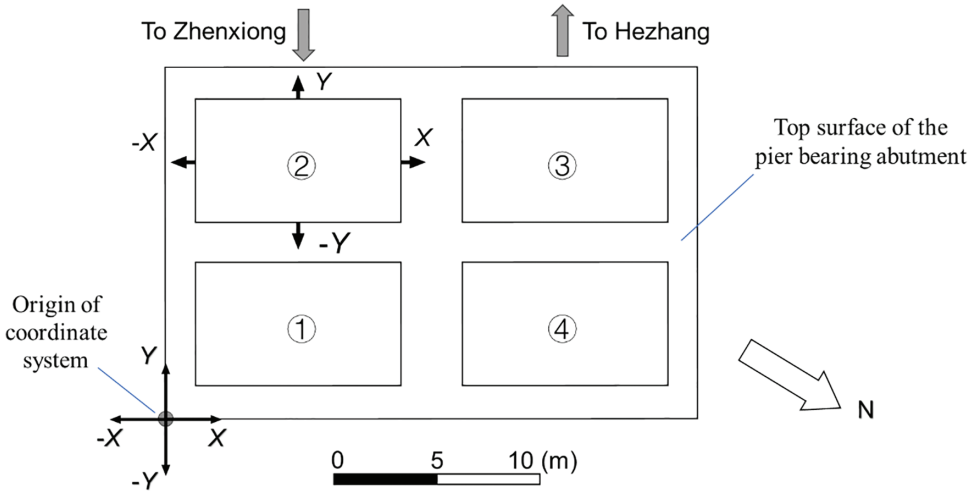

Figure 6: Sub-Pier numbering and local observation coordinate system of the main pier of the Zhaidi River Bridge

3.1.2 Mesh Grid Division of Bridge Pier

Test calculations by the bridge pier numerical models of different mesh grid style units (mainly two styles, tetrahedral grid, and hexahedral grid) show that under the default mesh grid size of ANSYS, the temperature fields and deformation fields of the bridge pier calculated by the models of different mesh grid styles are not much different. Therefore, the hexahedron-dominant mesh grid division is used in the numerical model of the bridge. This type of mesh model has high computational efficiency and is widely used in engineering.

In order to understand the influence of grid unit size on the simulation results, three bridge pier numerical models with different mesh grid unit sizes are used to simulate the temperature fields and temperature-induced deformation fields of the bridge pier under the low temperature and low radiation conditions in winter. The model mesh grid division and simulation calculation results are shown in Table 1.

There is no unified criterion for evaluating the impact of mesh grid division of numerical model on the calculation results. It is usually determined through convergence analysis of the calculation results. First, define the relative error (E_r) of the calculation results before and after the change in mesh grid size:

$$E_r = \frac{|R_{fine} - R_{coarse}|}{R_{coarse}} \times 100\%$$

where, R_{fine} represents the calculation result after the mesh grid size is reduced (refining), and R_{coarse} represents the calculation result before the mesh grid size is reduced (before refining). The Relative Error (E_r) is the variation rate of the calculation result after the mesh grid size is reduced relative to

the calculation result before the mesh grid size reduced. The commonly allowed range for E_r is 1% to 5%. Considering the limitation of simulation computation and computing resources, we choose 5% as the convergence criterion.

Table 1: Mesh grid size sensitivity simulation results of bridge pier model

Mesh grid division				Analyzing results			
Grid style	Grid side length	Number of nodes	Number of grid units	Temperature of bridge pier (max)	Relative error (E_r)	Total displacement of bridge pier (max)	Relative error (E_r)
Hex dominant	2 m	128,441	61,933	35.857°C		5.8554×10^{-2} m	
Hex dominant	1 m	296,618	138,340	32.553°C	9.21%	5.9141×10^{-2} m	1.00%
Hex dominant	0.50 m	1,549,016	726,317	31.17°C	4.25%	5.9398×10^{-2} m	0.43%

Note: In the default mesh grid size model, the number of nodes is 128,456 and the number of grid units is 61,935.

It can be seen from Table 1 that when the grid size (side length) is refined from 2 m to 1 m, the relative error E_r of the temperature calculation results is 9.21%, which is greater than 5% and does not meet the required convergence criterion. However, when the gride size is further reduced to 0.5 m, the E_r between the temperature calculated with the model of grid size of 0.5 m and the temperature calculated with the model of grid size of 1 m is 4.25%, less than 5%, which has met the convergence criterion. For the calculation of pile elastic deformation, the relative error (E_r) caused by grid size does not exceed 1%. Based on the temperature calculation and deformation calculation results, the mesh grid size of 1 m meets the convergence criterion.

In summary, this paper will adopt hexahedron-dominant mesh grid division with grid side length 1 m for the numerical model of the main pier of the Zhaidihe Bridge.

3.1.3 Material Parameters of Bridge Pier Model

The pier body is constructed using C40 concrete, and the material parameters used in the numerical simulation are listed in Table 2.

Table 2: Material parameters for the numerical model of the main pier of the Zhaidi River Bridge

Density (ρ) [21]	2400 kg/m	**Thermal conductivity (k)** [25]	1.5 $W \cdot m^{-1} \cdot °C^{-1}$
Elastic modulus (E) [21]	32.5 GPa	**Specific heat capacity (c)** [25]	900 $J \cdot kg^{-1} \cdot °C^{-1}$
Poisson's ratio (ν) [21]	0.2	**Thermal expansion coefficient (α)** [26,27]	$10 \times 10^{-6} °C^{-1}$

The values for the density (ρ) and elastic mechanical parameters (E, ν) of C40 concrete are relatively consistent in relevant literatures, but there are certain variations in the values of thermodynamic parameters (k, c, α), as shown in Table 3 [25–27].

Table 3: The value range of thermodynamic parameters for C40 concrete

Parameter	Range of values	Typical value (*used in paper*)	Unit
Thermal conductivity (k)	1.0∼2.0	1.5	$W{\cdot}m^{-1}{\cdot}°C^{-1}$
Specific heat capacity (c)	800∼1000	900	$J{\cdot}kg^{-1}{\cdot}°C^{-1}$
Thermal expansion coefficient (α)	7×10^{-6}∼13×10^{-6}	10×10^{-6}	K^{-1} or $°C^{-1}$

The sensitivity analysis on the effects of three material thermodynamic parameters: Thermal Conductivity (k), Specific Heat Capacity (c), and Thermal Expansion Coefficient (α) on numerical simulation results are conducted in this paper. The material parameter sensitivity analysis is performed by follow way: The investigated material parameter varies within its value range, and the other two parameters remain unchanged; Observe the response of the bridge pier to the ambient temperature variation when the value of the investigated parameter changes, to understand the sensitivity of the temperature response of the bridge pier to the investigated parameter. Numerical simulation method is used to carry out parameter sensitivity analysis. In the analysis, 5 sample values of the investigated parameter for sensitivity analysis, including the minimum and maximum values, are taken at equal intervals within the value range of the parameter, while the other two parameters remain unchanged (the values of the unchanged thermodynamic parameters are taken as the Typical Value listed in Table 3, that is, $k=1.5\ W{\cdot}m^{-1}{\cdot}°C^{-1}$, $c=900\ J{\cdot}kg^{-1}{\cdot}°C^{-1}$, $\alpha=10\times10^{-6}°C^{-1}$). The temperature field and temperature-induced deformation field of the bridge pier under low temperature and low radiation condition in winter are simulated with these parameter values. The maximum temperature (T_{max}) and the maximum temperature-induced deformation total displacement ($D_{t\ max}$) of the bridge pier relative to the variations of the investigated parameters extracted from simulation results are listed in Tables 4–6. According to the results listed in Tables 4–6, scatter plots are drawn (Simulated), and linear fitting is performed on each scatter plot, as shown in Figs. 7–12.

Table 4: Sensitivity simulation results of the thermal conductivity k

Thermal conductivity k ($W{\cdot}m^{-1}{\cdot}°C^{-1}$)	1	1.25	1.5	1.75	2
Maximum temperature of pier body T_{max} (°C)	34.994	33.638	32.467	31.512	30.776
Maximum total displacement of pier $D_{t\,max}$ (m)	0.0558	0.05749	0.05895	0.06021	0.06131

Note: In the simulation calculation, $c=900\ J{\cdot}kg^{-1}{\cdot}°C^{-1}$, $\alpha=10\times10^{-6}°C^{-1}$.

Table 5: Sensitivity simulation results of the specific heat capacity c

Specific heat capacity c ($J{\cdot}kg^{-1}{\cdot}°C^{-1}$)	800	850	900	950	1000
Maximum temperature of pier body T_{max} (°C)	32.766	32.591	32.467	32.329	32.166
Maximum total displacement of pier $D_{t\,max}$ (m)	0.06059	0.05974	0.05895	0.05821	0.05753

Note: In the simulation calculation, $k=1.5\ W{\cdot}m^{-1}{\cdot}°C^{-1}$, $\alpha=10\times10^{-6}°C^{-1}$.

Table 6: Sensitivity simulation results of the thermal expansion coefficient α

Thermal expansion coefficient α (°C^{-1})	7×10^{-6}	8.5×10^{-6}	10×10^{-6}	11.5×10^{-6}	13×10^{-6}
Maximum temperature of pier body T_{max} (°C)	32.467	32.467	32.467	32.467	32.467
Maximum total displacement of pier $D_{t\,max}$ (m)	0.04175	0.05035	0.05895	0.06755	0.07616

Note: In the simulation calculation, $k = 1.5$ W·m^{-1}·°C^{-1}, $c = 900$ J·kg^{-1}·°C^{-1}.

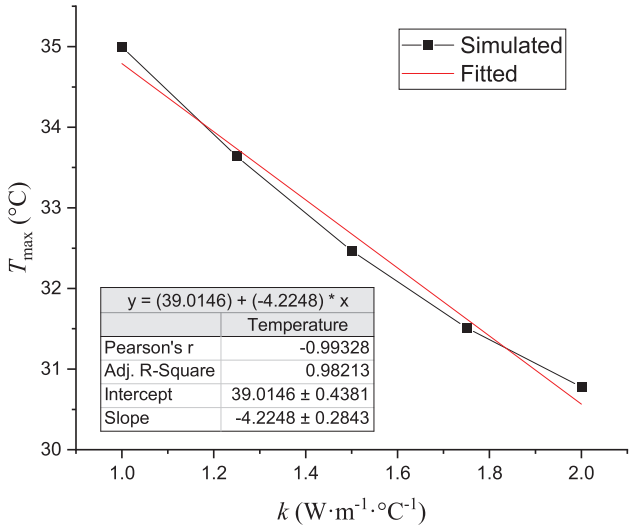

Figure 7: The relationship curve of the maximum pier temperature (T_{max}) vs thermal conductivity coefficient (k). The black dots are the simulation results (Simulated), and the red line is the linear fitting function curve (Fitted)

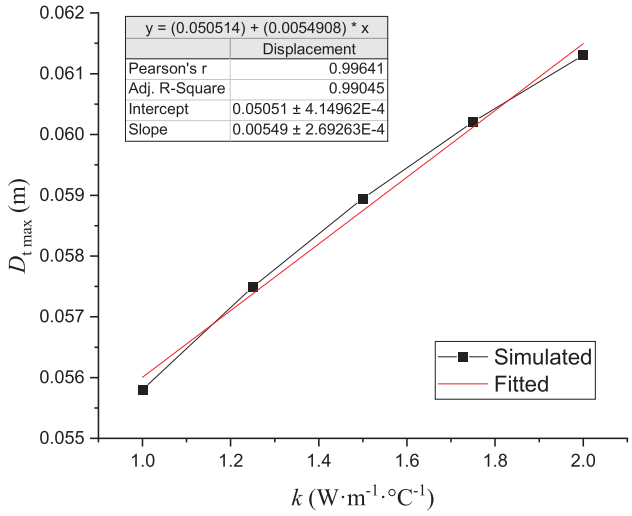

Figure 8: The relationship curve of the temperature-induced maximum total displacement of the pier ($D_{t\,max}$) vs. thermal conductivity coefficient (k). The black dots are the simulation results (Simulated), and the red line is the linear fitting function curve (Fitted)

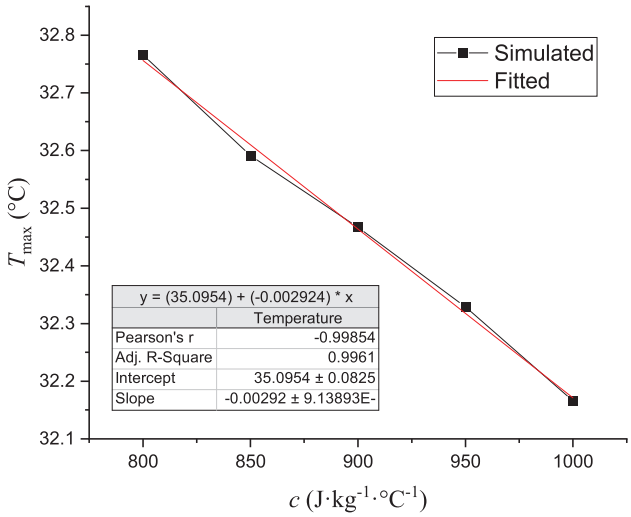

Figure 9: The relationship curve of the maximum pier temperature (T_{max}) vs. the specific heat capacity (c). The black dots are the simulation results (Simulated), and the red line is the linear fitting function curve (Fitted)

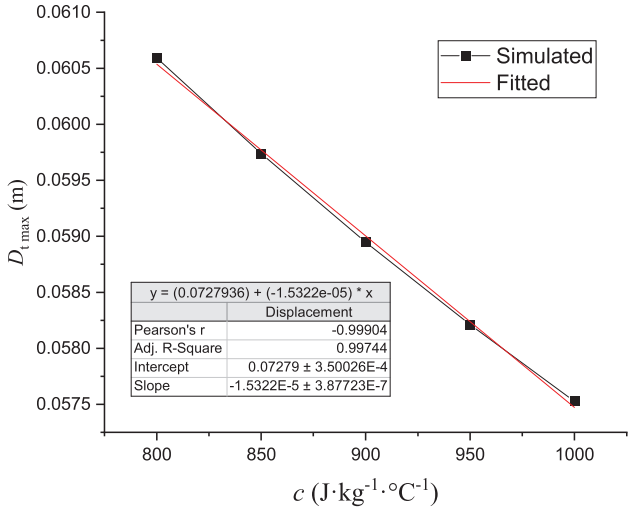

Figure 10: The relationship curve of the temperature-induced maximum total displacement of the pier ($D_{t\,max}$) vs. the specific heat capacity (c). The black dots are the simulation results (Simulated), and the red line is the linear fitting function curve (Fitted)

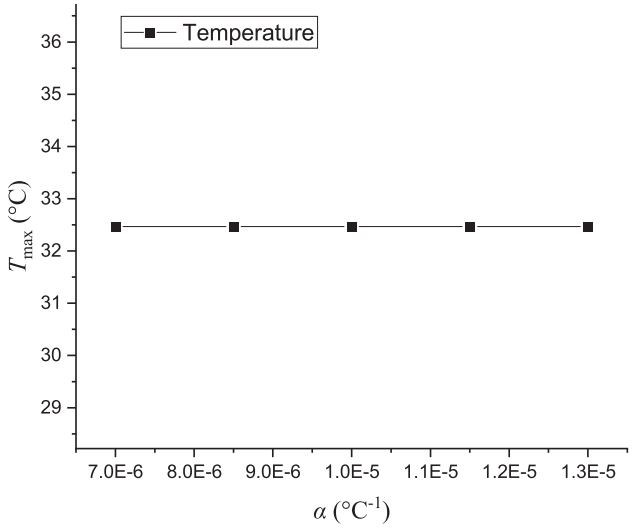

Figure 11: The relationship curve of the maximum pier temperature (T_{max}) vs. the thermal expansion coefficient (α)

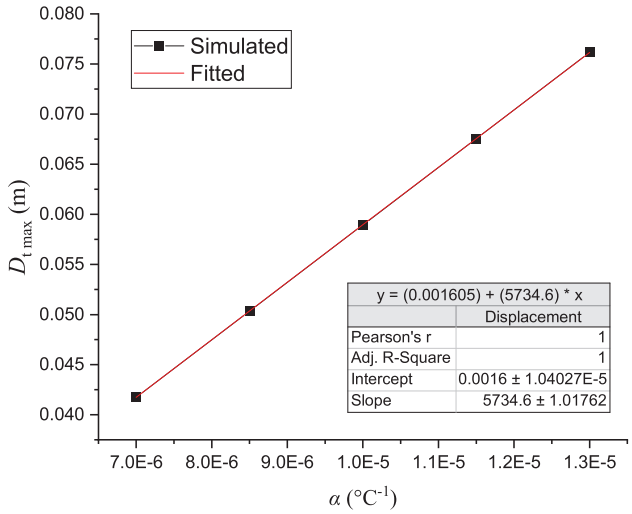

Figure 12: The relationship curve of the temperature-induced maximum total displacement of the pier ($D_{t\,max}$) vs. the thermal expansion coefficient (α). The black dots are the simulation results (Simulated), and the red line is the linear fitting function curve (Fitted)

Thermal Conductivity (*k*)

The simulation calculations are performed according to the five sample points of the thermal conductivity k, and the corresponding simulation results are shown in Table 4. The relationship curves of the maximum temperature T_{max} and the maximum total displacement $D_{t\,max}$ of the temperature-induced deformation of the bridge pier versus the thermal conductivity k drawn based on the data listed in Table 4 are shown in Figs. 7 and 8. As the thermal conductivity k increases, the maximum temperature (T_{max}) of the pier body decreases, while the maximum total displacement ($D_{t\,max}$) of the pier increases, and the variation patterns of T_{max}-k and $D_{t\ max}$-k are all close to linear.

***Specific Heat Capacity* (c)**

The simulation calculations are carried out according to the five sample points of the specific heat capacity c, and the corresponding simulation results are shown in Table 5. The relationship curves of the maximum temperature T_{max} and the maximum total displacement $D_{t\,max}$ of the temperature-induced deformation of the bridge pier versus the specific heat capacity c drawn based on the data listed in Table 5 are shown in Figs. 9 and 10. As the specific heat capacity c increases, the maximum temperature (T_{max}) of the pier body slightly decreases, and the maximum total displacement ($D_{t\,max}$) of the pier also decreases. The variation patterns of T_{max}-c and $D_{t\ max}$-c are all close to linear.

***Thermal Expansion Coefficient* (α)**

The simulation calculations are carried out according to the five sample points of the thermal expansion coefficient α, and the corresponding simulation results are shown in Table 6. The relationship curves of the maximum temperature T_{max} and the maximum total displacement $D_{t\,max}$ of the temperature-induced deformation of the bridge pier versus the thermal expansion coefficient α drawn based on the data listed in Table 6 are shown in Figs. 11 and 12. As the thermal expansion coefficient α increases, the maximum temperature (T_{max}) of the pier body remains unchanged, while the maximum total displacement ($D_{t\,max}$) of the pier increases significantly in a completely linear manner, with a correlation of 100% with the linear fitting curve.

3.2 Constitutive Relationship of Pier Deformation

Analysis of the bridge pier deformation caused by wind force and temperature variation inevitably involves the stress-strain relationship of the pier material. In a temperature-steady environment, under the premise that the pier material does not yield, linear elastic constitutive relationship can be applied to the pier deformation caused by wind force. When the ambient temperature varies, the pier material will expand or contract with the temperature variation. The temperature-induced deformation is superimposed on the linear elastic deformation caused by wind force, resulting in stress variation in the pier body.

3.2.1 Physical Equation

In general, wind force and temperature variation coexist in a natural environment. Considering the superposition of wind force and temperature variation, the constitutive relationship (physical equation) of the bridge pier can be expressed as Eq. (1):

$$\begin{cases} \varepsilon_x = \frac{1}{E}\left[\sigma_x - \nu\left(\sigma_y + \sigma_z\right)\right] + \alpha \cdot \Delta T = \varepsilon_{xW} + \varepsilon_T \\ \varepsilon_y = \frac{1}{E}\left[\sigma_y - \nu\left(\sigma_z + \sigma_x\right)\right] + \alpha \cdot \Delta T = \varepsilon_{yW} + \varepsilon_T \\ \varepsilon_z = \frac{1}{E}\left[\sigma_z - \nu\left(\sigma_x + \sigma_y\right)\right] + \alpha \cdot \Delta T = \varepsilon_{zW} + \varepsilon_T \\ \gamma_{xy} = \frac{1}{\mu} \cdot \tau_{xy} = \gamma_{xyW}, \gamma_{yz} = \frac{1}{\mu} \cdot \tau_{yz} = \gamma_{yzW}, \gamma_{zx} = \frac{1}{\mu} \cdot \tau_{zx} = \gamma_{zxW} \end{cases} \tag{1}$$

In the equation above, σ_x, σ_y, σ_z, τ_{xy}, τ_{yz}, τ_{zx} represent the stress components, where σ_x, σ_y and σ_z are normal stresses, and τ_{xy}, τ_{yz} and τ_{zx} are shear stresses. ε_x, ε_y, ε_z, γ_{xy}, γ_{yz}, γ_{zx} represent the strain components, where ε_x, ε_y and ε_z are normal strains, and ε_{xW}, ε_{yW} and ε_{zW} represent the deformations of the pier caused by wind force, and $\varepsilon_T = \alpha \cdot \Delta T$ represents the temperature-induced deformations of the pier due to temperature variation. γ_{xy}, γ_{yz}, γ_{zx} represent the shear strains, which are independent of temperature-induced deformation and are caused by wind force, so they can be written as γ_{xyW}, γ_{yzW}, γ_{zxW}. ΔT is the temperature variation, measured in K or °C; α is the coefficient of linear expansion,

representing the strain per unit temperature variation, with units of 1/K or 1/°C; v is the Poisson' s ratio of the material; and E is the elastic modulus of the material.

3.2.2 Geometric Equation

Let the displacement vector generated by the deformation of the pier material be denoted as $\vec{R} = \{u, v, w\}$, then the strain components in Eq. (1) and the displacement components u, v and w are determined by Eq. (2).

$$\begin{cases} \varepsilon_x = \dfrac{\partial u}{\partial x},\ \varepsilon_y = \dfrac{\partial v}{\partial y},\ \varepsilon_z = \dfrac{\partial w}{\partial z} \\ \gamma_{xy} = \dfrac{\partial v}{\partial x} + \dfrac{\partial u}{\partial y} \\ \gamma_{yz} = \dfrac{\partial w}{\partial y} + \dfrac{\partial v}{\partial z} \\ \gamma_{zx} = \dfrac{\partial u}{\partial z} + \dfrac{\partial w}{\partial x} \end{cases} \tag{2}$$

Additionally, in the expressions for the first three normal strain components (ε_x, ε_y, ε_z) in Eq. (1), the temperature-induced deformation term is included. However, the expressions for the three shear strain components (γ_{xy}, γ_{yz}, γ_{zx}) do not include the temperature-induced deformation term. This indicates that the thermal expansion and contraction caused by temperature variation in homogeneous materials result in normal strains (volume expansion or contraction), but do not cause shear deformation. When $\Delta T = 0$, the temperature is steady, therefore no temperature-induced deformation occurs. So, Eq. (1) clarifies the physical mechanism of the pier deformation caused by the coupling action of wind force and temperature variation.

Considering the wind forces in the natural environment of the Zhaidi River bridge, the elastic stress field of the main pier body is calculated according to the principles of elastic mechanics; Additionally, the ambient temperature variations of the pier are obtained as according to the climate and sunshine conditions, furthermore the temperature distribution variations within the pier body are determined in the light of the heat conduction theory. The constitutive relationship in Eq. (1) is used to obtain the wind-induced deformation (ε_{xW}, ε_{yW}, ε_{zW}, γ_{xyW}, γ_{yzW}, γ_{zxW}) and temperature-induced deformation (ε_{xT}, ε_{yT}, ε_{zT}) of the pier. Further using the geometric relationships in Eq. (2), the displacement components (u, v, w) of the pier can be inversely derived from the strain components (ε_x, ε_y, ε_z, γ_{xy}, γ_{yz}, γ_{zx}). The above theory can provide a basis for the deformation analysis of the pier after construction.

3.3 Wind Force and Temperature Variation Conditions (Environmental Boundary Conditions of the Bridge Pier)

The airflow (wind force), air temperature and sunshine (temperature variation) around the pier acting on the surface of the pier constitute the specific boundary conditions of the wind-induced deformation and temperature-induced deformation of the pier. These conditions trigger responses governed by the constitutive relationship outlined in Eq. (1), resulting in the deformation of the pier. Consequently, it is crucial having a comprehensive understanding of the potential airflow patterns and temperature variations (working conditions) in the environment of a high bridge pier. Such insight enables the identification of appropriate boundary conditions corresponding to varying wind and temperature working conditions. This step is vital for accurately simulating and analyzing the impact of wind force and temperature variation on the deformation of the pier after construction.

3.3.1 *Wind Force*

The wind force generated by airflow around a bridge pier in the form of wind load (wind pressure) on the surface of the bridge pier constitute the wind force boundary condition for wind-induced deformation of the bridge pier. In addition to the obvious factor of the pier height, the airflow velocity (wind speed) and airflow direction (wind orientation) in the environment around the bridge pier are two critical factors that determine the wind force (wind pressure) exerted on the surface of the bridge pier.

Wind Speed and Height

According to the Industry Standard of the People' s Republic of China JTG D60-2004 "General Specifications for Design of Highway Bridges and Culverts" [20], wind loads can be converted into static loads and applied to the bridge piers. In consideration of the design basic wind speed (v_{10}), the wind load (wind pressure) is determined by Eq. (3):

$$f_{\mathrm{W}} = k_0 k_1 k_3 \cdot \frac{\gamma}{2g} \cdot (k_2 k_5 \cdot v_{10})^2 \tag{3}$$

In the formula above, f_{W} represents the standard value of the cross-bridge wind load (wind pressure), measured in kPa; $k_0 = 1$ is the conversion coefficient for the design wind speed recurrence period for super-large bridges; $k_1 = 1.5$ is the wind resistance coefficient, which is related to the geometric size of the bridge pier; $k_3 = 1.4$ is the terrain and geographical conditions coefficient for mountain pass conditions; $\gamma = 0.012017e^{-0.0001 \cdot Z}$ is the gravitational density of air, with the unit kN/m^3; Z is the height above the ground or water surface, measured in meters; g is the gravity acceleration, taken as 9.8 m/s^2; k_2 is a correction coefficient that accounts for ground surface roughness, gradient winds, and wind speed variation with height (v-Z), with specific values determined according to the height Z above the ground or water surface (see Table 7); $k_5 = 1.7$ is the gust wind speed coefficient for hilly terrain with significant undulations; and v_{10} is the design basic wind speed in the area of the bridge site (the maximum wind speed for a 50-year recurrence according to the statistical analysis of 10-min average wind speeds observed at a height of 10 m above flat, open ground in the area) [28].

Table 7: Wind speed correction coefficient k_2 corresponding to height Z (values for canyon site conditions) [20]

Z/m	k_2	Z/m	k_2	Z/m	k_2	Z/m	k_2
5	1.00	20	1.12	50	1.29	80	1.40
10	1.00	30	1.19	60	1.33	90	1.42
15	1.07	40	1.25	70	1.36	100	1.45

As indicated by Eq. (3), when the location of the bridge site is fixed, the wind load is determined exclusively by the wind speed v_{10} and the height Z. With the increase of the bridge height Z, the wind pressure f_{W} correspondingly rises. For the Zhaidi River Bridge, the design reference wind speed is established at $v_{10} = 28.2$ m/s, aligning with a wind force scale 10 of the Beaufort scale. According to the Beaufort wind force scale [29], relative to the wind scale 10, the wind speed $v_{10} = 24.5$–28.4 m/s, and the wind pressure $f_{\mathrm{W}} = 0.41$–0.55 kPa. In order to explore the influence of wind speed on the deformation of constructed bridge pier, the simulation also accounts for the situations of wind scale 8 (wind speed $v_8 = 17.2$–20.7 m/s, 20.5 m/s is taken; wind pressure $f_{\mathrm{W}} = 0.20$–0.29 kPa) and wind scale 12 (wind speed $v_{12} = 32.7$–36.9 m/s, 36.5 m/s is taken; wind pressure $f_{\mathrm{W}} = 0.73$–0.93 kPa). The variation

in wind load (wind pressure) with height Z for the above three wind speed levels (v_8, v_{10}, v_{12}) is depicted in Fig. 13.

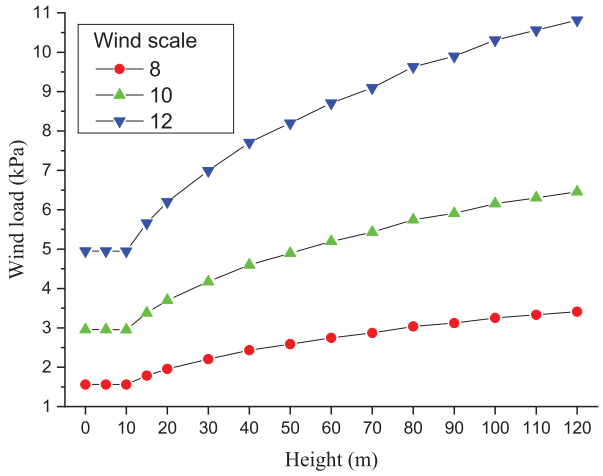

Figure 13: Variation of wind load with height for three wind speed scenarios (Wind scale 8, 10, and 12)

Wind Direction

The wind load is predominantly borne by the windward side surfaces of the pier (wind force action surfaces), while wind load on the leeward side surfaces of the pier can be reasonably disregarded. As illustrated in Fig. 14, the included angle between the transverse direction (X-axis direction) of the Zhaidi River Bridge and the orientation of the valley is about 20°. Each sub-piers of the main pier have two windward surfaces, the X-face and the $-Y$-face, facing the north wind coming from north to south along the valley (the wind direction is consistent with the orientation of the valley). In the numerical simulation, wind pressure only needs to be applied on the two windward side surfaces ($f_w \neq 0$), while no wind pressure needs to be applied on the two leeward side surfaces ($f_w = 0$).

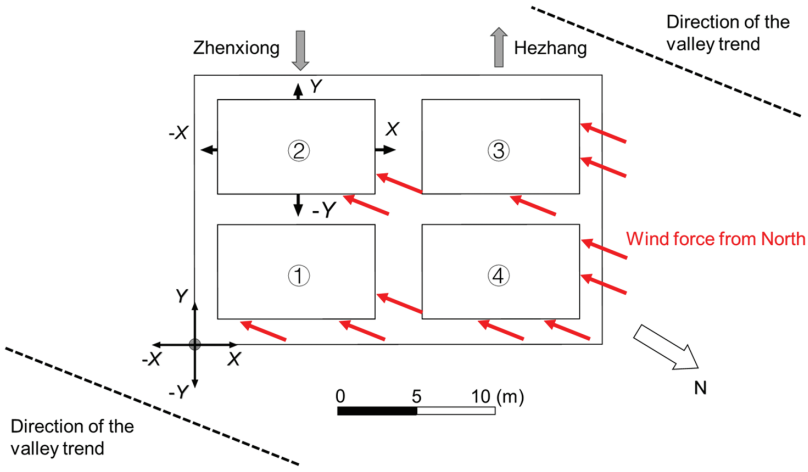

Figure 14: Schematic of the wind force boundary conditions on Pier 2# (main pier) of the Zhaidi River Bridge (for north wind as an example)

In addition, wind direction has other two effects on the wind forces acting on the pier surfaces: One is the shielding effect of the windward piers in a multi-sub-pier composite bridge pier on the airflow; The other is the intensity variation of the normal wind force and tangential wind force on the pier surface caused by the oblique intersection of the airflow direction (wind direction) and the pier surfaces.

The shielding of airflow by the windward piers in a multi-sub-pier combined bridge pier will weaken the intensity of wind force acting on the leeward piers. Taking the working conditions shown in Fig. 14 as an example: The X-side surface is one of the windward surfaces of the pier. The wind load applied to the X-side surface is primarily borne by Sub-Pier ④ and Sub-Pier ③. Due to the shielding effect of Sub-Piers ④ and ③, the wind load intensities on the X-side surfaces of Sub-Pier ① and Sub-Pier ② are significantly reduced. The $-Y$-side surface is another windward surface of the pier. The wind load applied to the $-Y$-side surface is mainly borne by Sub-Pier ① and Sub-Pier ④. As a result of the shielding effect of Sub-Piers ① and ④, the wind load intensities on the $-Y$-side surfaces of Sub-Pier ② and Sub-Pier ③ are also reduced. The reduction in wind load intensities on the shielded windward surfaces of the leeward piers can be described using a shielding coefficient (χ), also referred to as the wind load intensity reduction factor ($0 < \chi \leq 1$). Thus, the wind load intensities on the shielded windward surfaces of the leeward piers can be expressed as $\chi \cdot f_{\mathrm{W}}$. *The primary goal of the simulation is to evaluate the maximum impact of wind load on the deformation of the constructed piers*. Consequently, the simulation prioritizes the wind load effects on the windward piers, while the degree of wind load reduction on the leeward piers is of secondary importance. As long as the wind load effect on the leeward piers can be distinguished from that on the windward piers, the simulation will meet its requirements. To reflect this, the shielding coefficient for the windward surfaces of the windward piers is set to $\chi = 1.0$, while that for the windward surfaces of the leeward piers is assigned a value of $\chi = 0.5$.

The angle between the wind direction and the outer normal of the windward surface of the bridge pier is defined as the wind force action angle, denoted by θ. Then the normal wind force acting on the pier surface is given by $f_{\mathrm{Wn}} = f_{\mathrm{W}} \cdot \cos\theta$, and the tangential wind force is $f_{\mathrm{Wt}} = f_{\mathrm{W}} \cdot \sin\theta$. When the wind direction is parallel to the normal of the pier surface ($\theta = 0°$), the normal wind force is at its maximum ($f_{\mathrm{Wn}} = f_{\mathrm{W}}$) and the tangential wind force is at its minimum ($f_{\mathrm{Wt}} = 0$). When the wind direction is perpendicular to the normal of the pier surface ($\theta = 90°$), the normal wind force is at its minimum ($f_{\mathrm{Wn}} = 0$) and the tangential wind force is at its maximum ($f_{\mathrm{Wt}} = f_{\mathrm{W}}$). Assuming the frictional effects between the airflow and the pier surface are negligible, only the normal wind force (wind pressure) contributes to the deformation of the pier, whereas the tangential wind force has no significant impact. Consequently, the analysis of the pier surface focuses solely on the normal wind force.

Building on the preceding analysis, the wind load (**wind force boundary conditions**) applied to the windward side surfaces of each pier in the wind-induced deformation simulation of Pier 2# (the main pier) of the Zhaidi River Bridge can be determined using Eq. (4):

$$f_{\mathrm{Wn}} = \chi \cdot f_{\mathrm{W}} \cdot \cos\theta \tag{4}$$

In this context, f_{W} is calculated using Eq. (3). For instance, under the working conditions depicted in Fig. 14, the wind load on the windward side surfaces (wind force action surfaces) of each sub-pier is detailed in Table 8.

Table 8: Wind force boundary conditions on each sub-pier of Pier 2# (main pier) of the Zhaidi River Bridge (north wind)

Sub-Pier no.	Wind force action surface	Wind force action angle θ	Shielding coefficient χ	Wind load/kPa
①	X	20°	0.5	$f_{\mathrm{Wn}} = 0.5 \cdot f_{\mathrm{W}} \cdot \cos 20°$
	$-Y$	70°	1.0	$f_{\mathrm{Wn}} = f_{\mathrm{W}} \cdot \cos 70°$
②	X	20°	0.5	$f_{\mathrm{Wn}} = 0.5 \cdot f_{\mathrm{W}} \cdot \cos 20°$
	$-Y$	70°	0.5	$f_{\mathrm{Wn}} = 0.5 \cdot f_{\mathrm{W}} \cdot \cos 70°$
③	X	20°	1.0	$f_{\mathrm{Wn}} = f_{\mathrm{W}} \cdot \cos 20°$
	$-Y$	70°	0.5	$f_{\mathrm{Wn}} = 0.5 \cdot f_{\mathrm{W}} \cdot \cos 70°$
④	X	20°	1.0	$f_{\mathrm{Wn}} = f_{\mathrm{W}} \cdot \cos 20°$
	$-Y$	70°	1.0	$f_{\mathrm{Wn}} = f_{\mathrm{W}} \cdot \cos 70°$

3.3.2 Temperature Variation

The heat exchange between the bridge pier and the surrounding natural environment induces the temperature variations of the bridge pier surface. The heat generated by heat exchange on the pier surface is further diffused into the pier body via *heat conduction*, driving dynamic shifts in the spatial distribution of pier temperature (temperature field) and dynamic temperature differences at different positions in the pier body. These variations in the pier body, in turn, trigger corresponding temperature-induced deformation processes of the pier body. Thus, the heat exchange between the pier surface and the natural environment establishes the thermodynamic boundary condition for the temperature-induced deformation of the bridge pier. The heat exchange between the pier surface and the natural environment mainly comes from sunlight (solar thermal radiation) and the temperature difference between the air and the pier surface, corresponding to *two distinct types of heat transfer: thermal radiation and thermal convection*.

Thermal Radiation

Thermal radiation refers to the electromagnetic waves emitted by the thermal motion of particles within a substance. Any material with a temperature above absolute zero will emit thermal radiation [30]. While objects radiate thermal energy outward, they also absorb energy radiated from other objects. According to the Stefan-Boltzmann Law [31], the radiant thermal energy (q_{r}) emitted or absorbed by an object is directly proportional to the fourth power of the absolute surface temperature (T_{r}) of the object, expressed as Eq. (5):

$$q_{\mathrm{r}} = \varepsilon \sigma T_{\mathrm{r}}^{4} \tag{5}$$

In the equation: q_{r} represents the radiant thermal energy passing through a unit area per unit time, also referred to as the radiant heat flux density, which indicates the intensity of thermal radiation, and whose unit is $\mathrm{J \cdot s^{-1} \cdot m^{-2}}$ or $\mathrm{W \cdot m^{-2}}$. T_{r} is the absolute surface temperature of the object emitting or absorbing thermal radiation, with units in Kelvin (K). σ is the Stefan-Boltzmann constant, $\sigma = 5.670374419\ldots \times 10^{-8}\ \mathrm{W \cdot m^{-2} \cdot K^{-4}}$; ε is the emissivity of the object (a thermodynamic property of the material, also known as the radiation efficiency, dimensionless), where $0 \leq \varepsilon \leq 1$, $\varepsilon = q_{\mathrm{r}}/q_{\mathrm{rb}}$, where q_{rb} is the radiation intensity of a black body (an ideal substance that absorbs all wavelengths of

radiant heat and is in thermal equilibrium), and q_r is the radiation intensity of a general material (gray body), where $q_r < q_{rb}$.

For the main pier of the Zhaidi River Bridge, what is considered is the influence of solar radiation on the bridge pier, and the mutual radiation between the surfaces of the sub-piers can be neglected. Solar radiation energy (q_r) is diffused and propagated using electromagnetic waves as carriers, and is attenuated by various factors during the propagation process. The solar radiation that reaches the earth shines on the earth' s surface in the form of sunlight. The surface of any object exposed to sunlight will heat up due to the reception of solar radiation energy. Due to the change in the incident direction of sunlight caused by the rotation and revolution of the earth, the actual solar radiation intensity ($q_{sr\ in}$) received by any engineering object on the ground will vary depending on the space where the project is located (geographical latitude, the relationship between the surface of the object and the incident direction of sunlight, etc.) and time (four seasons of the year, 24 h a day). Peng [32] (page 27–33) details the calculation method for solar radiation. Using this method, the diurnal variation of solar radiation intensity on the main pier of the Zhaidi River Bridge under two extreme climatic conditions in summer and winter is calculated, and the calculated result is shown in Fig. 15, which depicts the daily variation of solar radiation intensity ($q_{sr\ in}$) received by each side surface of the main pier of the Zhaidi River Bridge during the summer solstice and the winter solstice for 24 h a day. It is evident that due to the change in *the solar elevation angle* at different times of the year, the solar radiation intensity on the four side surfaces of the bridge pier varies significantly.

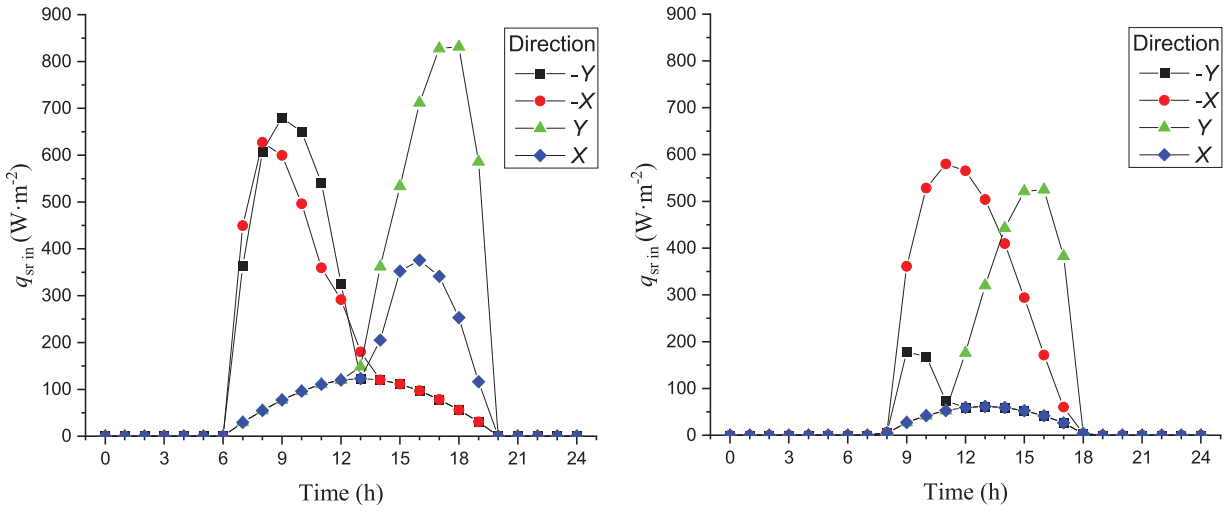

(**a**) Summer (**b**) Winter

Figure 15: Daily variation curves of solar radiation intensity on the main pier surfaces of the Zhaidi River Bridge during the seasons summer (**a**) and winter (**b**)

As shown in Fig. 15a, during the summer solstice, the sunshine time in the region where the bridge is located is from 06:00 to 20:00, and the sunshine time is nearly 13 h. The solar radiation received by each side surface of the bridge pier is extremely uneven, which is the fundamental cause of temperature-induced deformation of the pier. Compared with Fig. 8, the azimuth of the $-Y$ axis is about 30°north of east, the azimuth of the $-X$ axis is about 30°east of south, the azimuth of the Y axis is about 30°south of west, and the azimuth of the X axis is about 30°west of north. Therefore, the $-Y$ and $-X$ faces receive solar radiation first. As time progresses, around 13:00 Beijing time, the sun is positioned

directly south. At the summer solstice, the sunshine time is the longest and the solar radiation is also the strongest. Additionally, the bridge site is close to the Tropic of Cancer, so at the summer solstice, the direction of the sunshine is almost perpendicular to the ground at noon, the solar radiation intensity on all sides of the bridge pier will decrease, and the radiation intensity received by each side surface is also very close. In the afternoon, the Y and X surfaces begin to receive sunlight.

As shown in Fig. 15b, during the winter solstice, the sunshine time at the bridge site is from just after 08:00 to 18:00, with less than 11 h of sunlight. Compared with Fig. 15a, it can be observed that the solar radiation intensity during the winter solstice is much weaker than that during the summer solstice, and the peak value is 26.6% lower than that during the summer solstice. Additionally, during the winter solstice, the solar elevation angle is the smallest of the year. Shortly after sunrise, the sunlight will shift from the $-Y$ side to the $-X$ side. Unlike the summer solstice, the sunlight obliquely hits the bridge piers at noon in winter, so the afternoon solar radiation gradually shifts from the $-X$ side to the Y side, while the X side of the pier is hardly exposed to sunlight.

Thermal Convection

The heat exchange between the surface of the bridge pier and the surrounding air can be described by the convection heat transfer equation as shown by Eq. (6):

$$q_c = -h_c \cdot (T_s - T_a) \tag{6}$$

In the equation: q_c represents the heat exchanged by the thermal convection between the pier surface and the air around, through the unit area per unit time (heat flux density), measured in $W \cdot m^{-2}$. h_c is the convective heat transfer coefficient, measured in $W \cdot m^{-2} \cdot K^{-1}$. T_s is the surface temperature of the bridge pier, measured in K. T_a is the temperature of the air surrounding the pier, measured in K. Since there is a linear relationship between Kelvin and Celsius, the temperature difference ($\Delta T = T_s - T_a$) in the formula is the same regardless of whether the temperature unit is K or °C.

The symbol "−" before the expression on the right side of the equal sign in Eq. (6) indicates that heat always flows towards the side with the lower convective surface temperature. Specifically: when $T_s < T_a$, $q_c > 0$, heat flows from the surrounding air into the pier; when $T_s > T_a$, $q_c < 0$, heat flows from the pier to the surrounding air; and when $T_s = T_a$, $q_c = 0$, there is no heat exchange between the pier and the surrounding air. The convective heat transfer coefficient h_c between the concrete bridge pier and the surrounding air is determined by Eq. (7):

$$h_c = 2.60 \left(\sqrt[4]{|T_a - T_s|} + 1.54v \right) \tag{7}$$

In the equation, the symbols T_a and T_s have the same meaning as in Eq. (6). v represents the wind speed. It is evident that the convection heat transfer coefficient depends not only on the temperature difference between the air and the pier surface but also on the wind speed. As wind speed increases, the convection heat transfer coefficient also increases. Therefore, when performing numerical simulations of temperature-induced deformation of the bridge pier, the convective heat transfer coefficient h_c should be adjusted according to the wind speed. This reflects the coupling effect of two natural loads: wind and temperature.

Atmospheric temperature is influenced by multiple factors, however, on clear days with solar radiation, the daily temperature variation exhibits a well-defined pattern, which can be typically described by a sinusoidal curve [33–35]. Uder the temperature conditions corresponding to summer and winter seasons as shown in Fig. 15, the typical daily variation curves of the Zhaidi River Bridge site in the extreme high temperature weather in summer and the extreme low temperature weather in

winter are determined based on historical meteorological data as shown in Fig. 16 [36]. As can be seen from Fig. 16, no matter in summer or winter, the lowest temperature of the day occurs at 3am and the highest temperature occurs at 14 p.m. Although the calculated temperatures may differ by 2°C–3°C at certain times, concrete structures are relatively insensitive to such temperature changes. As a result, the error in the calculated structural temperature differences is smaller than the error in the temperature data itself [32]. There is a clear contrast between summer and winter temperatures: in summer, the minimum temperature is around 16°C, and the maximum reaches 31°C, giving a daily temperature range of 15°C; in winter, however, the minimum temperature drops to −9°C, and the maximum can rise only to 11°C, but resulting in a larger daily temperature range of 20°C.

Thermodynamic Boundary Conditions Involving Thermal radiation and Thermal Convection Simultaneously

Thermal radiation and thermal convection exist simultaneously in the natural environment of the bridge site. These two physical processes are superimposed, coupled, and influence each other on the pier surface, forming the thermodynamic boundary conditions of the pier. While the pier surface receives solar radiation (absorbs heat), it also emits thermal radiation (releases heat) to the surrounding environment, thus changing the air temperature. Heat absorption makes the pier surface temperature rise, while heat release makes it drop. The superposition of heat absorption and heat release will form a relatively balanced pier surface temperature. The variation in pier surface temperature due to thermal radiation will also affect the temperature difference between the pier surface and the surrounding air, thereby affecting the heat convection between the pier and the air. The superposition, coupling and mutual influence of thermal radiation and thermal convection alter the thermal energy on the pier surface, thus forming a new pier surface temperature.

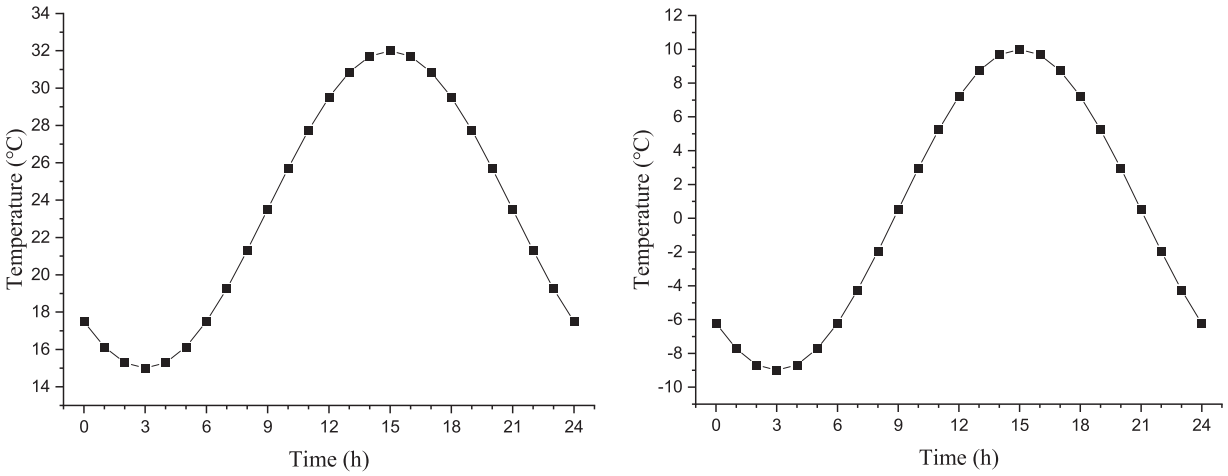

(**a**) Summer (**b**) Winter

Figure 16: Typical daily temperature variation curves in the Zhadi River Bridge site area in summer (a) and in winter (b)

According to the above description of the physical processes of thermal radiation and thermal convection occurring on the pier surface, the thermodynamic boundary condition on the pier surface can be expressed by Eq. (8):

$$q_s = q_{sr} + q_{sc} = -\varepsilon\sigma \cdot \left(T_s^4 - T_r^4\right) - h_c \cdot (T_s - T_a) \tag{8}$$

In the equation, T_s represents the surface temperature of the pier, which is the result of the combined effects of thermal radiation and convection; T_r is the temperature generated by the radiation heat absorbed by the pier surface; T_a is the air temperature surrounding the pier; q_s is the heat flux density generated on the pier surface due to the superposition of thermal radiation and thermal convection; ε is the emissivity of the pier, which is taken as $\varepsilon = 0.9$ in numerical simulations [32]; σ is the Stefan-Boltzmann constant; h_c is the convective heat transfer coefficient determined by Eq. (7); $q_{sr} = -\varepsilon\sigma \cdot \left(T_s^4 - T_r^4\right)$ is the residual radiation heat energy generated on the pier surface due to radiation heat absorption ($q_{sr\,in} = \varepsilon\sigma T_r^4$) and heat release ($q_{sr\,out} = \varepsilon\sigma T_s^4$); $q_{sc} = -h_c \cdot (T_s - T_a) = -h_c \cdot \Delta T_{sa}$ is the heat flux density passing through the pier surface via heat convection, where $\Delta T_{sa} = T_s - T_a$ is the temperature difference between the pier surface and the surrounding air. The units for the thermal energy (heat flux density q_s, q_{sr}, q_{sc}) are $W \cdot m^{-2}$, and the units for temperature (T_s, T_r, T_a) are K. The radiation heat exchange and convective heat exchange on the pier surface are considered positive for heat absorption and negative for heat release.

Since the physical mechanisms of thermal radiation and thermal convection are different, their heat exchange processes and the effects on temperature are also different. The physical mechanism of thermal radiation is electromagnetic radiation, which does not rely on the contact between the heat-emitting and heat-absorbing materials, nor does it depend on the existence of materials that receive the radiated heat energy. As long as the emitting material itself has a temperature above absolute zero, the thermal radiation can be generated. This determines that the absorption and release of radiant heat are relatively independent processes. The absorption of thermal radiation by the pier is passive, and the intensity of the absorbed radiation ($q_{sr\ in}$) is determined by the surface temperature of the Sun and the influences of solar radiation electromagnetic waves during propagation (such as sunlight orientation, scattering, absorption, etc.). The absorbed thermal radiation will produce a corresponding temperature (T_r) on the pier surface. On the other hand, the thermal radiation of the pier is active, and the intensity of the emitted thermal radiation ($q_{sr\ out}$) is determined by the pier surface temperature (T_s). The physical mechanism of thermal convection is the collision of elementary particles between different materials excited by thermal motion. Therefore, the simultaneous existence and mutual contact of the two materials that release heat and absorb heat are necessary conditions for the occurrence of thermal convection. Moreover, the temperature difference ($\Delta T_{sa} = T_s - T_a \neq 0$) between the two materials is a sufficient condition for thermal convection, where ΔT_{sa} is the driving force for thermal convection between the pier and the surrounding air.

Based on the analysis of the two heat transfer mechanisms—thermal radiation and convective heat transfer—and their primary controlling factors, the thermal radiation and temperature environment conditions of the main pier of the Zhaidi River Bridge shown in Figs. 15 and 16 can be substituted into the thermodynamic boundary conditions for the temperature-induced deformation of the bridge pier, as described in Eq. (8). This results in *two working conditions of ambient temperature variation: high temperature and high radiation in summer, and low temperature and low radiation in winter*.

The daily variation process values of absorbed solar radiation heat on each side surface of the main pier of the Zhaidi River Bridge in summer and winter for 24 h $q_{sr\ in} = q_{sr\ in}(t)$ shown in Fig. 15 are taken as the targets of numerical simulation, and are substituted into the absorption radiation heat equation $q_{sr\ in} = \varepsilon\sigma T_r^4$ to determine the daily variation processes of the radiation heat temperature $T_r = T_r(t)$ produced by ambient environment (which is primarily due to solar radiation) on each side surface of the pier.

The 24-h air temperature variation process values in summer and winter shown in Fig. 16 are taken as the daily variation process $T_a = T_a(t)$ of the ambient air temperature around the pier body in the numerical simulation.

During simulation, the bridge pier had not yet been constructed, so among the three temperatures (T_s, T_r, T_a) in boundary condition Eq. (8), only the surface temperature of the pier, $T_s = T_s(t)$, had no measured values. In numerical simulation, an appropriate initial value, $T_s = T_{s0}$, is assigned to the pier surface temperature. Then, using the boundary condition with the initial pier surface temperature assigned, the heat conduction of the pier body is simulated repeatedly with a cycle of 24 h. In the simulation of the pier thermodynamic process, thermal convection, thermal radiation, and the conduction of boundary heat flow to the interior of the pier will make the pier temperature field $T(x, y, z, t)$ and the pier surface temperature $T_s(t)$ vary dynamically. The variation of the pier surface temperature $T_s(t)$ will in turn make the convective heat transfer coefficient h_c and the thermal radiation intensity $q_{sr\ out}$ emitted from the pier surface vary synchronously, thereby triggering a new round process of thermal convection and thermal radiation on the pier surface as well as heat conduction within the pier body. This process cycle is repeated until the heat exchange process on the pier surface and the heat conduction process inside the pier body reach a dynamic equilibrium (i.e., a stable heat flow field is formed between the pier surface and the interior of the pier), thus forming a relatively stable pier body temperature field $T(x, y, z, t)$.

The physical mechanism and logical relationship of the heat exchange process between the bridge pier and the surrounding environment are shown in Fig. 17.

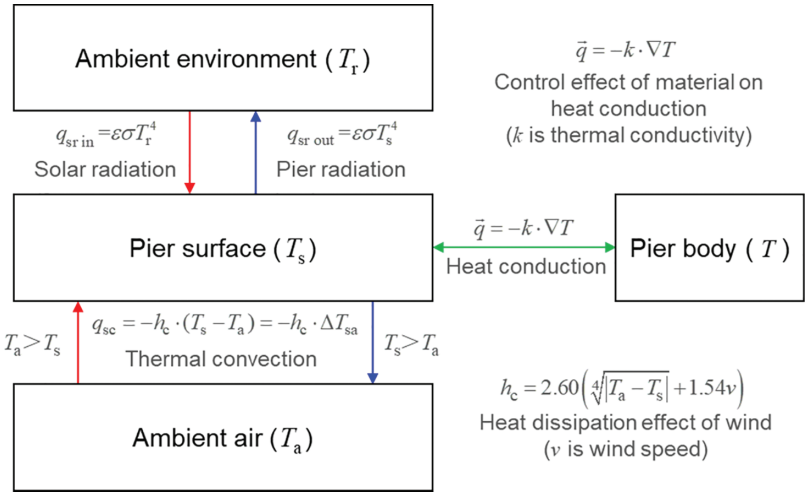

Figure 17: Illustration of the physical mechanism and logical relationship of the heat exchange process between the bridge pier and the surrounding environment

3.4 Response of the Bridge Pier to Wind Force and Temperature Variation

The wind forces and temperature variations on the pier surface constitute two types of boundary conditions for the pier body, namely, the wind force boundary conditions listed in Table 3 (with north wind as an example) and the temperature (thermodynamic) boundary conditions shown in Eq. (8). The wind forces and temperature variations on the pier surface led to two distinct deformation mechanisms of the pier body: wind-induced deformation and temperature-induced deformation, reflecting the response of the pier to these two types of boundary conditions.

3.4.1 Response of the Pier to Wind Force

The wind force is applied to the surface of the bridge pier in the form of wind loads listed in Table 3 (north wind as an example). The wind loads on the pier surfaces vary with wind direction, wind speed, and height. A completed bridge pier but one that has not yet been connected to the upper bridge structure can be likened to a cantilever beam subjected to a non-uniform load under the action of wind force. The root of the pier (the junction with the pier foundation pedestal) is equivalent to the fixed end of the cantilever beam, while the top of the pier (which may have an unfinished upper structure) can be likened to the free end of the cantilever beam.

Deformation Response of the Pier to Wind Force

On the premise that the pier body remains an elastic working state (without damage or failure), the pier will respond to the wind load with the elastic deformation (ε_{xW}, ε_{yW}, ε_{zW}, γ_{xyW}, γ_{yzW}, γ_{zxW}) in Eq. (1). The wind load will cause the pier to experience horizontal lateral displacement perpendicular to the height (Z-axis) direction and varying with the height, with the largest lateral displacement at the top and the smallest at the root. The non-uniform lateral displacement causes the pier to tilt and bend in the wind direction, resulting in changes in the verticality of the pier.

Internal Force Response of the Pier to Wind Force

The wind load acting on the boundaries will generate elastic stresses (σ_x, σ_y, σ_z, τ_{xy}, τ_{yz}, τ_{zx}) within the pier body. The lateral deformation of the pier caused by the wind force induces shear forces that vary with height in the cross-sections of the pier at different heights. Additionally, the inclined bending of the pier in the downwind direction will generate bending moments that vary with height on cross-sections perpendicular to the pier axis. The bending moment is smallest at the top and largest at the root, and the direction of the bending moment is consistent with the bending direction of the pier. The bending moment causes the cross-sections of the pier to experience normal stress. The nature and magnitude of the normal stress vary along the wind direction. The tensile stress is the largest near the surface on the windward side of the pier, while the compressive stress is the largest near the surface on the leeward side. Between the tensile and compressive stress distribution areas, there is a neutral axis perpendicular to the wind direction and with zero normal stress.

3.4.2 Response of the Pier to Temperature Variation

As previously mentioned, temperature variation of materials is a manifestation of thermal exchange of the materials. According to the thermodynamic boundary condition of the pier as shown in Eq. (8), the result of the heat exchange between the pier and the surrounding environment is that the pier surface obtains thermal energy (heat flux density) q_s and its corresponding pier surface temperature T_s. The pier responds to the heat flux density obtained on the pier surface via heat conduction—the thermal energy generated by thermal radiation and thermal convection on the surface of the pier is further conducted within the pier, forming a dynamically varying temperature field T (x, y, z, t). The pier surface temperature T_s, as a component of the pier temperature field, also varies with the pier temperature field, thus forming a dynamic pier surface temperature T_s (t). It can be said that the heat conduction process inside the pier is an integral part of the heat exchange between the pier and the surrounding environment. The thermal radiation and thermal convection on the pier surface (boundary) and the heat conduction within the pier constitute a complete process of heat exchange between the bridge pier and the surrounding environment (see Fig. 17).

Heat conduction follows Fourier' s Law of Heat Conduction, which states that heat flows from areas of higher temperature to those of lower temperature, and the amount of heat flowing in a

direction is proportional to the temperature decrease in that direction [37], that is:

$$\vec{q} = -k \cdot \nabla T \tag{9}$$

In the equation, k is the thermal conductivity coefficient (always defined to be positive [38]), which reflects the ability of materials for heat conduction (a physical property of materials [38]), and its SI unit is $W{\cdot}m^{-1}{\cdot}K^{-}$), $\nabla T = \left(\frac{\partial T}{\partial x}, \frac{\partial T}{\partial y}, \frac{\partial T}{\partial z}\right)$ is the temperature gradient ($\nabla = \vec{i}\frac{\partial}{\partial x} + \vec{j}\frac{\partial}{\partial y} + \vec{k}\frac{\partial}{\partial z}$is the Hamiltonian operator). ∇T indicates the direction along which the temperature variation rate within the material body is the maximum, and the magnitude $|\nabla T|$ represents the spatial temperature variation rate in the direction of the temperature gradient, and its unit is $K{\cdot}m^{-1}$. $\vec{q}$ is the heat flux density vector, which points opposite to the temperature gradient (i.e., heat always flows from higher temperature to lower temperature). The value of the heat flux density is denoted by $q = \left|\vec{q}\right|$ with unit $W{\cdot}m^{-2}$.

In an isotropic homogeneous medium without heat sources, the temperature field T (x, y, z, t) generated by heat conduction satisfies the heat conduction equation expressed by Eq. (10a) [39]:

$$\rho c \frac{\partial T}{\partial t} = -\nabla \cdot \vec{q} = k \cdot \nabla^2 T \tag{10a}$$

In the equation, ρ represents the density of the medium, with unit $kg{\cdot}m^{-3}$; c is the specific heat capacity of the medium, with unit $J{\cdot}kg^{-1}{\cdot}K^{-1}$; and $\nabla^2 = \nabla{\cdot}\nabla = \frac{\partial^2}{\partial x^2} + \frac{\partial^2}{\partial y^2} + \frac{\partial^2}{\partial z^2}$ is the Laplacian operator. When the heat conduction in the medium reaches a steady state, $\frac{\partial T}{\partial t} = 0$, thus the heat conduction equation degenerates into the Laplace Equation as shown by Eq. (10b).

$$\nabla^2 T = 0 \tag{10b}$$

According to the physical principle of heat conduction described by Eqs. (9)–(10b) and the temperature-induced deformation described by Eq. (1) ($\varepsilon_T = \alpha \cdot \Delta T$), the bridge pier will respond to variations in the ambient temperature in terms of both temperature and deformation.

Temperature Response

The heat conduction equation expressed by Eq. (10a)) shows that when the bridge pier is invaded by the pier surface heat flux q_s (corresponding to the pier surface temperature T_s) determined by the thermodynamic condition Eq. (8), the heat flux diffusion process $\vec{q}$ (t) described in Eq. (10a) will occur inside the pier, and a dynamic temperature field T (x, y, z, t) corresponding to the heat diffusion process will generated within the pier. This is the thermodynamic response of the pier to the variation in the ambient temperature. When the ambient temperature remains constant for a period, the heat exchange between the pier and the environment will gradually reach a dynamic equilibrium process (marked by $\frac{\partial T}{\partial t} = 0$). Consequently, the temperature field inside the pier body also enters a stable state described by Eq. (10b), no longer varies with time, and forms an equilibrium temperature field T_E (x, y, z, t).

Deformation Response

The temperature response of the pier to the variation of the ambient temperature leads to temperature variation of each point within the pier, thereby forming a dynamic temperature field T (x, y, z, t) of the pier. Corresponding to a relatively stable ambient temperature, there will also be a corresponding equilibrium temperature field T_E (x, y, z, t). The temperature field of the pier

generated by the temperature response causes temperature differences between points in the pier medium space, forming a temperature difference distribution $\Delta T\,(x, y, z, t)$ within the pier, and further generating a corresponding temperature-induced deformation field $\varepsilon_{\mathrm{T}}\,(x, y, z, t) = \alpha \cdot \Delta T\,(x, y, z, t)$. The temperature differences between the surfaces of the pier will lead to differences in the temperature-induced deformation at different parts of the pier. The difference between the temperature-induced deformation at different parts of the pier will inevitably cause the variation in the verticality of the bridge pier.

3.5 Reliability Verification of the Numerical Model for the High Bridge Pier of the Zhaidi River Bridge

During the construction process, the construction company monitored the displacement of the main pier of the Zhaidi River Bridge. The horizontal displacement monitoring data of the main pier (2# pier) of the Zhaidi River Bridge on December 29, 2019 is utilized to verify the reliability of the numerical model of the high bridge pier of the Zhaidi River Bridge established in our paper.

3.5.1 Measured Displacements of a Monitored Point on the Top of the Main Pier of the Zhaidi River Bridge

As shown in Fig. 18, the monitored point selected was set at the midpoint of $-X$ side edge on the top surface of Sub-Pier ① of the Zhaidi River Bridge main pier. The coordinates $(X_{\mathrm{M}t},\ Y_{\mathrm{M}t})$ of the monitored point were measured at 08:00, 09:00, 12:00, 15:00, and 18:00, and the results are shown in Table 9. Using the coordinate of the monitored point at 08:00 $(X_{\mathrm{M8}},\ Y_{\mathrm{M8}})$ as the reference, the difference between the coordinate of the monitored point at other times $(X_{\mathrm{M}t},\ Y_{\mathrm{M}t})$ and the coordinate at 08:00 $(\Delta X_{\mathrm{M}t} = X_{\mathrm{M}t} - X_{\mathrm{M8}},\ \Delta Y_{\mathrm{M}t} = Y_{\mathrm{M}t} - Y_{\mathrm{M8}})$ represents the actual relative displacement of the monitored point on the bridge pier, as shown in Table 9.

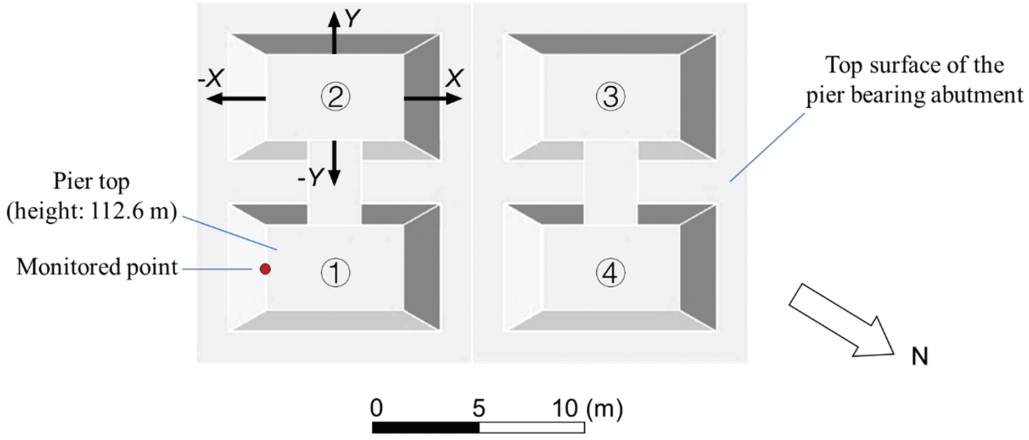

Figure 18: Location of a monitored point for pier deformation on the main pier of the Zhaidi River Bridge

Table 9: Measured coordinates and relative displacements of a monitored point for pier deformation of the main pier of the Zhaidi River Bridge

Time	Position of monitored point (m)		Measured Displacement (mm)	
	$X_{M\,t}$	$Y_{M\,t}$	$\Delta X_{M\,t} = X_{M\,t} - X_{M8}$	$\Delta Y_{M\,t} = Y_{M\,t} - Y_{M8}$
08:00	3,027,608.9890	486,419.8400	0	0
09:00	3,027,608.9893	486,419.8401	0.3	0.1
12:00	3,027,608.9897	486,419.8397	0.7	−0.3
15:00	3,027,608.9894	486,419.8389	0.4	−1.1
18:00	3,027,608.9890	486,419.8390	0	−1.0

Note: The monitored point coordinates (X_{Mt}, Y_{Mt}) in the table represent the measured coordinate values to the local coordinate system for the project, where the subscript 't' in the coordinate symbols indicates the corresponding observation time; The measured displacement refers to the relative displacement of the monitored point at different time (t) compared to its position at 8:00 ($\Delta X_{Mt} = X_{Mt} - X_{M8}$, $\Delta Y_{Mt} = Y_{Mt} - Y_{M8}$), where ($X_{M8}$, Y_{M8}) represents the coordinate of the monitored point at 08:00.

3.5.2 Comparison of Simulated and Measured Displacements of Monitored Point on the Top of the Main Pier of the Zhaidi River Bridge

According to historical weather records for the location of the Zhaidihe Bridge [40], the weather on 29 December, 2019 was cloudy, with a high temperature of 18°C, a low temperature of 1°C, and a light south wind with wind scale 1. The daily variation of solar radiation intensity on different sides of the bridge pier is considered following Fig. 15b in our manuscript, but the radiation intensity is appropriately reduced to account for the shading effect of clouds on a cloudy day. Numerical simulations of the variations in the temperature field and the displacement field of the bridge pier over time are conducted with the relevant environmental boundary conditions. Extract the displacement ($\Delta X_{St} = X_{St} - X_{S8}$, $\Delta Y_{St} = Y_{St} - Y_{S8}$) of the numerical model grid node corresponding to the monitored point shown in Fig. 18 on each hour on the hour from 08:00 to 18:00, and compare these values with the measured displacement values ($\Delta X_{Mt} = X_{Mt} - X_{M8}$, $\Delta Y_{Mt} = Y_{Mt} - Y_{M8}$) on the same time, as shown in Fig. 19 and Table 10.

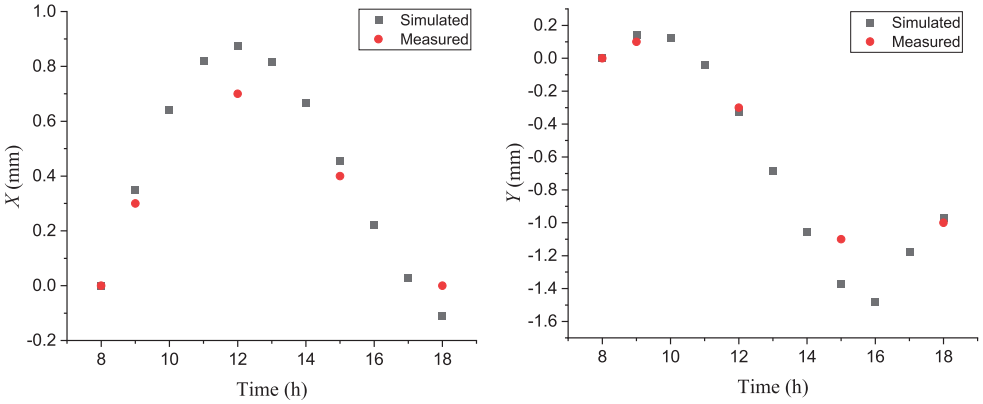

(**a**) X component (**b**) Y component

Figure 19: Comparison of simulated and measured displacements at monitored point on the main pier of the Zhaidi River Bridge: (a) X component; (b) Y component

Table 10: Comparison of simulated and measured displacements at monitored point on the main pier of the Zhaidi River Bridge

Time	X component of displacement (mm)		Y component of displacement (mm)	
	Simulated ΔX_{St}	Measured ΔX_{Mt}	Simulated ΔY_{St}	Measured ΔY_{Mt}
09:00	0.35	0.3	0.14	0.1
12:00	0.87	0.7	−0.32	−0.3
15:00	0.46	0.4	−1.37	−1.1
18:00	−0.11	0	−0.97	−1.0
RMSE	0.1098		0.1390	

As shown in Fig. 19 and Table 10, the simulated displacement and the monitored displacement exhibit similar trends and values in both the X and Y directions (the root mean square error for the X-component displacement is 0.1098, and the root mean square error for the Y-component displacement is 0.1390), and the variation magnitude of the simulated displacement is greater than that of the measured displacement (this means that implementing safety measures based on simulated displacement is safer). Thus, the reliability of the numerical model of the high pier of the Zhaidi River Bridge established in this paper is verified.

4 Numerical Simulation Analysis of Wind-Induced and Temperature-Induced Deformation of the High Bridge Pier of the Zhaidi River Bridge

This study conducts numerical simulations of the wind-induced deformation and the temperature-induced deformation of the constructed main pier of the Zhaidi River Bridge using the ANSYS Workbench simulation platform. The platform employs finite element analysis methods, integrating structural, thermal, fluid, electromagnetic and other analyses, and can conveniently and intuitively perform coupled analysis of multiple physical fields [41]. Considering the natural environment of the Zhaidi River Bridge site and the engineering characteristics of the bridge, under the premise that the pier is free from material and structural defects, this paper primarily focuses on the influences of wind force and temperature variation on the deformation of the bridge pier after construction. Assume the pier material is homogeneous and isotropic, and the pier structure meets the design requirements. Additionally, consider that the upper beam structure has been installed on the top of the constructed pier but has not yet been connected as a whole, and it is converted into a gravity load and applied on the top of the constructed pier. The wind force and temperature variation conditions, determined in Section 3.3 of this paper, are applied to the numerical model of the intact main pier of the Zhaidi River Bridge, as shown in Fig. 5. The numerical simulations of the wind-induced deformation, temperature-induced deformation, and wind-temperature coupling deformation of the main pier of the Zhaidi River Bridge are carried out, so as to provide a basis for exploring the influence of wind force and temperature variation on the deformation of high bridge piers after construction.

4.1 Numerical Simulation Analysis of the Influence of Wind Force on the Deformation of the High Bridge Pier after Construction

4.1.1 Wind Force Conditions

The magnitude of the wind force is primarily determined by the wind speed. To thoroughly assess the impact of wind force on the deformation of the bridge pier after construction, three wind speed levels (three working conditions) were selected: 1) wind speed of scale 8; 2) wind speed of scale 10 (design wind speed); and 3) wind speed of scale 12. Since the bridge is in a valley, the direction of the maximum wind force is basically along the valley orientation (approximately 350°, as shown in Fig. 14). Therefore, the influence of wind direction variation is no longer considered in the simulation study. The three wind force working conditions are applied to the high bridge pier model shown in Fig. 5 to simulate the wind-induced deformation of the high bridge pier after construction.

4.1.2 Wind-Induced Deformation Simulation Results of the High Bridge Pier

Fig. 20 shows the displacement cloud diagrams of the pier caused by a north wind with scale 8. The Y component of the displacement points to the positive Y direction, with the maximum displacement of 0.027 m occurring at the top of the pier. The X component of the displacement points to the negative X direction, with the maximum displacement of -0.052 m occurring also at the top of the pier. The direction of the horizontal displacement synthesized by X component and Y component is roughly the same as the wind direction. Due to the gravity load of the upper bridge structure, the Z component displacement of the pier points to the negative direction of Z-axis, with a maximum displacement of -0.0064 m, which has little impact on the overall displacement of the pier. The maximum value of all three composite displacement is 0.058 m, occurring at the top of Sub-Pier ④, and the displacement points to the 6th quadrant.

In the displacement distribution of the pier shown in Fig. 20, the maximum values of X component displacement, Y component displacement, and total displacement (i.e., the vector synthesis of the X, Y, and Z component displacements) of horizontal sections (including the four sub-pier cross-sections) at different heights of the pier in the height range from 0 to 110 m at intervals of 10 m are extracted as shown in Fig. 21. As shown in Fig. 21, with the increase of height, the variation trends of X component displacement, Y component displacement, and total displacement are similar. The deformation displacement of the pier caused by the wind force increases with height, and the increase trend of the pier displacement becomes more and more pronounced towards the top of the pier.

Fig. 22 shows a comparison between the variations of the three-component synthetic displacement of the bridge pier caused by three intensity levels of wind forces with scale 8, 10, and 12 with height. As can be seen from Fig. 22, the deformation displacement of the bridge pier caused by the north winds of scale 10 and 12 is similar to the result of the north wind of scale 8 (the direction of wind-induced deformation displacement of the pier is the same as the wind direction, and the displacement increases with the height of the pier, with the maximum displacement occurring at the top of the pier), and the only difference is that the faster the wind speed, the larger the deformation displacement value. Specifically, to the wind forces of scale 8, 10, and 12, the maximum wind-induced deformation displacements are 0.058 m, 0.110 m, and 0.185 m, respectively.

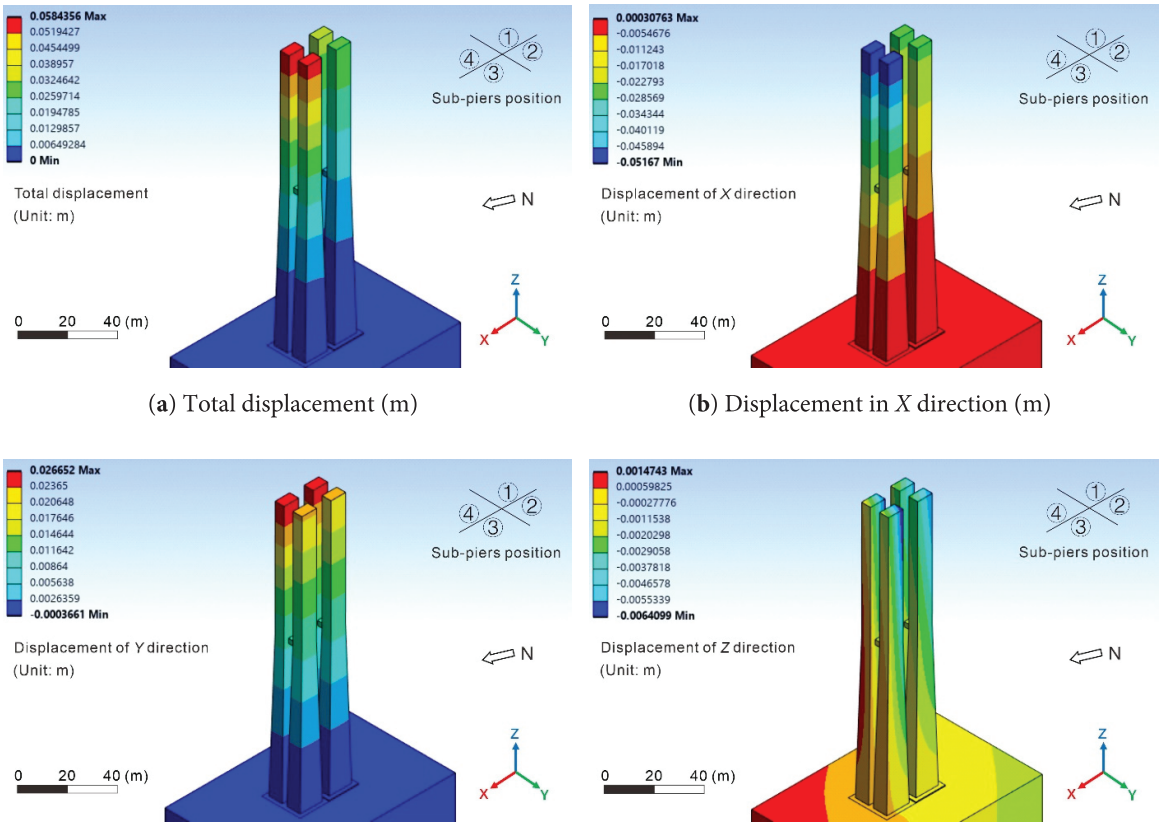

(**a**) Total displacement (m)

(**b**) Displacement in *X* direction (m)

(**c**) Displacement in *Y* direction (m)

(**d**) Displacement in *Z* direction (m)

Figure 20: Displacement cloud diagrams of the main pier of the Zhaidi River Bridge caused by a north wind with scale 8 (Unit of displacements noted in the figure is m): (a) Total displacement; (b) Displacement in *X* direction; (c) Displacement in *Y* direction; (d) Displacement in *Z* direction

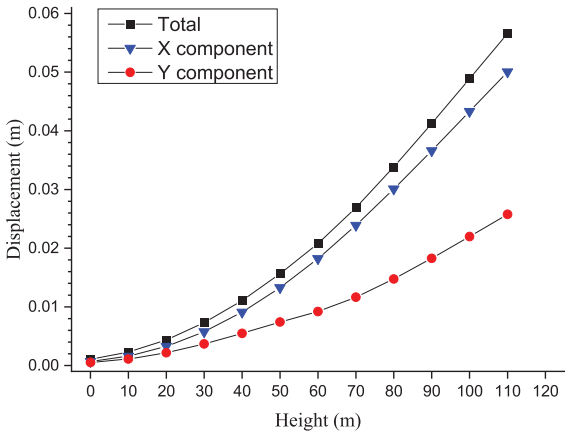

Figure 21: Variation of pier displacement with height under the influence of a north wind with scale 8 on the main pier of the Zhaidi River Bridge

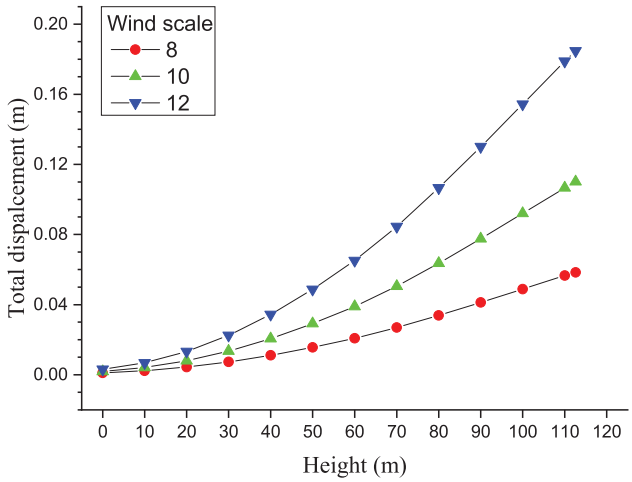

Figure 22: Comparison of the variation in the deformation total displacement with height of the main pier of the Zhaidihe Bridge caused by wind forces of scale 8, 10, and 12

4.2 Numerical Simulation of the Influence of Temperature Variation on the Deformation of the High Bridge Pier after Construction

4.2.1 Temperature Variation Conditions

In order to study the influence of temperature variation on the deformation of the high bridge pier after construction, without the wind force action, the two extreme temperature conditions shown in Figs. 15 and 16, *high temperature and high radiation condition in summer* (Figs. 15a and 16a), and *low temperature and low radiation condition in winter* (Figs. 15b and 16b), are applied to the high bridge pier model shown in Fig. 5 to simulate the temperature field and temperature-induced deformation of the high bridge pier.

4.2.2 Temperature Field Simulation Results of the High Bridge Pier

In order to reveal the temperature field of the pier body under different temperature working conditions, the horizontal cross-section, including the 4 cross-sections of Sub-Pier ①~Sub-Pier ④, of the main pier (Pier #2) at height 100 m is taken as an example to show the simulation results of the temperature filed. Fig. 23 shows the location of the horizontal cross-sections of the 4 sub-piers at height 100 m and the display of the sub-pier cross sections. Fig. 23a illustrates the specific position of these 4 sub-pier cross-sections on the bridge pier, while Fig. 23b shows the top-down view of the cross-section.

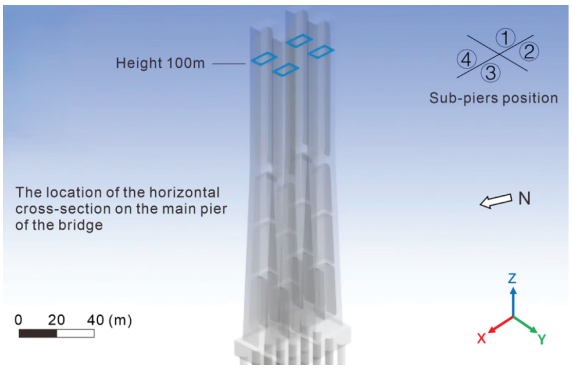

(**a**) The location of the horizontal cross-section on the main pier of the bridge

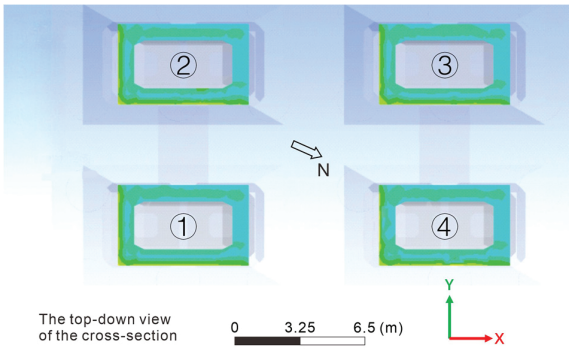

(**b**) The top-down view of the cross-section

Figure 23: Position of the horizontal cross-section of the Zhaidi River Bridge main pier at height 100 m (a) and display of four sub-pier cross-sections (b)

High Temperature and High Radiation Condition in Summer

The temperature fields of the horizontal cross-section of Sub-Pier ① at height 100 m are extracted at eight time points: 06:00, 09:00, 12:00, 15:00, 18:00, 21:00, 24:00, and 03:00 the following day, as shown in Fig. 24a–h.

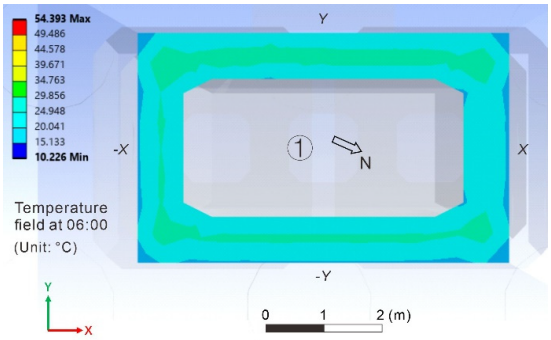

(**a**) Temperature field at 06:00

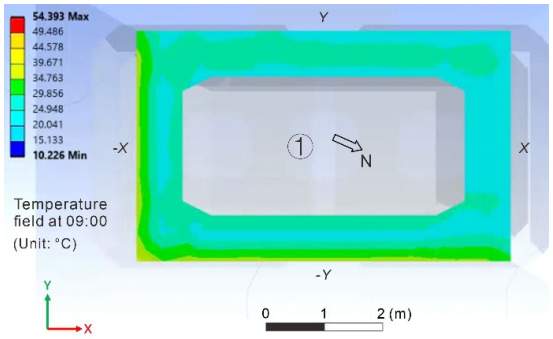

(**b**) Temperature field at 09:00

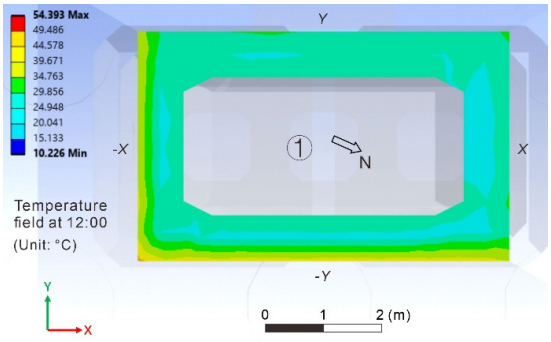

(**c**) Temperature field at 12:00

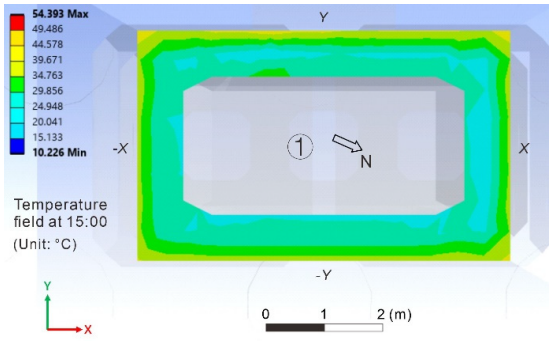

(**d**) Temperature field at 15:00

Figure 24: (Continued)

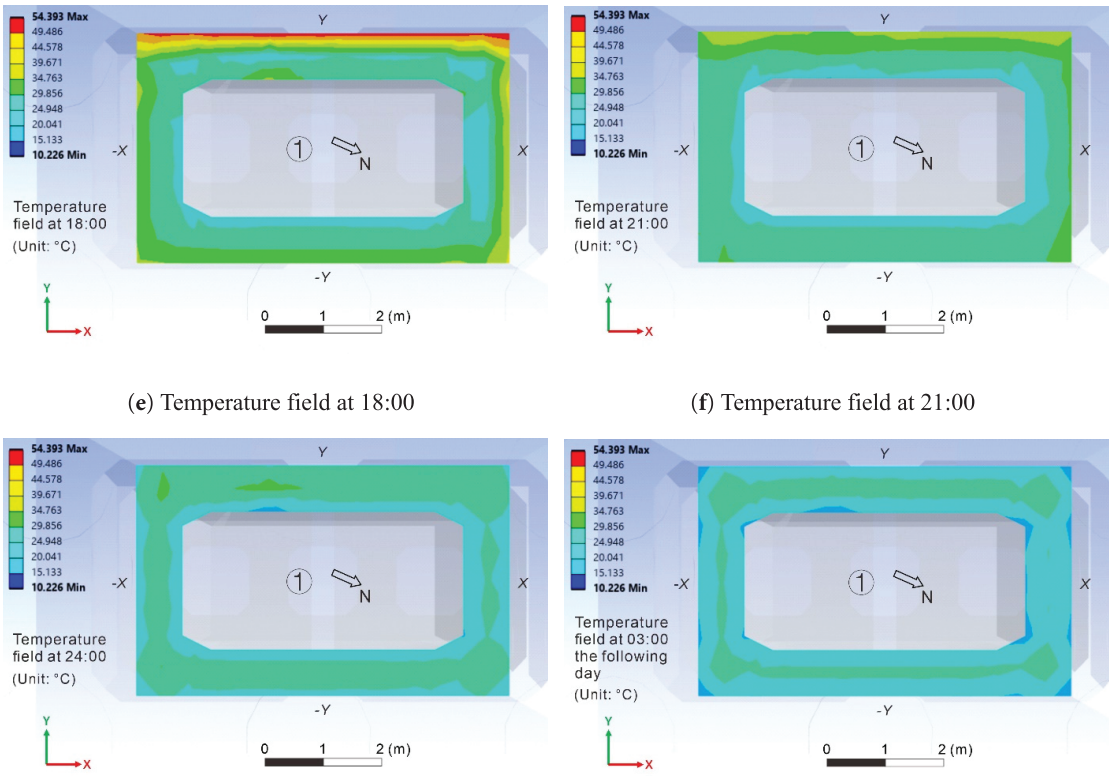

(**e**) Temperature field at 18:00

(**f**) Temperature field at 21:00

(**g**) Temperature field at 24:00

(**h**) Temperature field at 03:00 the following day

Figure 24: Temperature field cloud diagram of the horizontal cross-section Sub-Pier ① at the height 100 m on the main pier of the Zhaidi River Bridge under high temperature and high radiation condition in summer (Unit of temperatures in the figure is degree of Celsius): (a) Temperature field at 06:00; (b) Temperature field at 09:00; (c) Temperature field at 12:00; (d) Temperature field at 15:00; (e) Temperature field at 18:00; (f) Temperature field at 21:00; (g) Temperature field at 24:00; (h) Temperature field at 03:00 the following day

As can be seen from Fig. 24a, the atmospheric temperature is relatively low at 06:00 in the morning, and the temperature of the outer layer of the pier body is much lower than that of the inner layer, and the temperature difference reaches about 6°C to 10°C. However, the temperature distribution of the pier body is symmetrical at this time, and will not cause the verticality variation of the pier due to asymmetric temperature distribution. At 09:00 (Fig. 24b), the temperatures on the $-Y$ and $-X$ side surfaces of Sub-Pier ① begin to rise. At 12:00 (Fig. 24c), the temperatures on the $-Y$ and $-X$ side surfaces continue to rise, about 10°C higher than those on the other two sides, while the internal temperature of the pier also starts to rise. At 15:00 (Fig. 24d), the temperatures on the $-Y$ and $-X$ side surfaces begin to drop, while the temperature on the Y side surface begins to rise. At 18:00 (Fig. 24e), the temperature on the Y side surface reaches 54°C, nearly 20°C higher than those on the other three sides. At 21:00 (Fig. 24f), the sun has already set, and the surface temperature of the Y side has begun to drop, however, the internal temperature of the pier on the Y side is still rising due to heat conduction. By 24:00 (Fig. 24g), the convective heat exchange caused by the lower external atmospheric temperature results in a continuous decrease in the surface temperature of the

pier, and the thermal energy stored within the pier during the day is gradually lost. By 03:00 the next day (Fig. 24h), the temperatures on the four outer surfaces of the pier are almost uniform, approaching to the temperature distribution state observed at 06:00 the previous day (Fig. 24a). It is easy to find that the variation of the temperature field of the pier over time has a good correspondence with the daily variation of the solar radiation intensity on each side surface of the pier as shown in Fig. 15a.

Low Temperature and Low Radiation Condition in Winter

By the temperature field simulation results of the horizontal cross-section at the height of 100 m of Sub-Pier ① of the Zhaidi River Bridge main pier at 06:00, 09:00, 12:00, 15:00, 18:00, 21:00, 24:00, and 03:00 the following day (Fig. 25) as examples again, the daily variation of the pier temperature field under low temperature and low radiation condition in winter is observed.

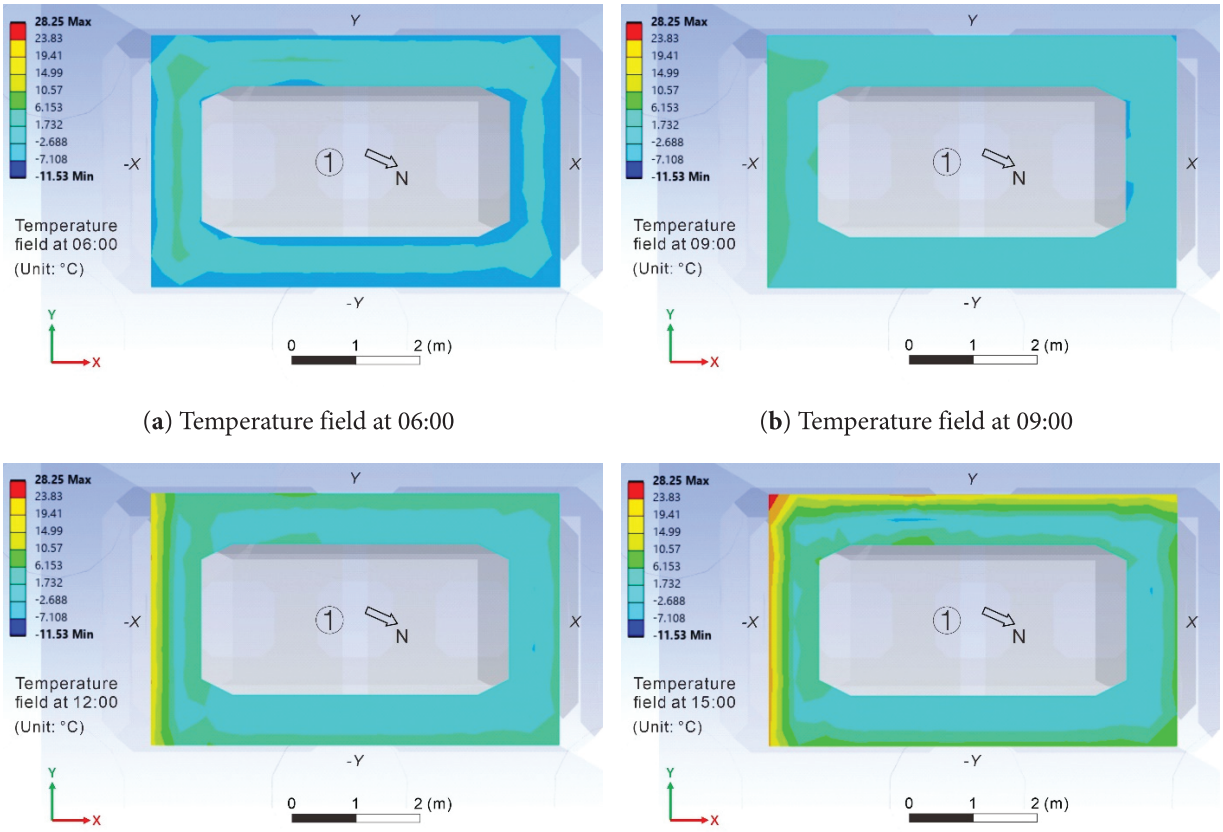

(**a**) Temperature field at 06:00

(**b**) Temperature field at 09:00

(**c**) Temperature field at 12:00

(**d**) Temperature field at 15:00

Figure 25: (Continued)

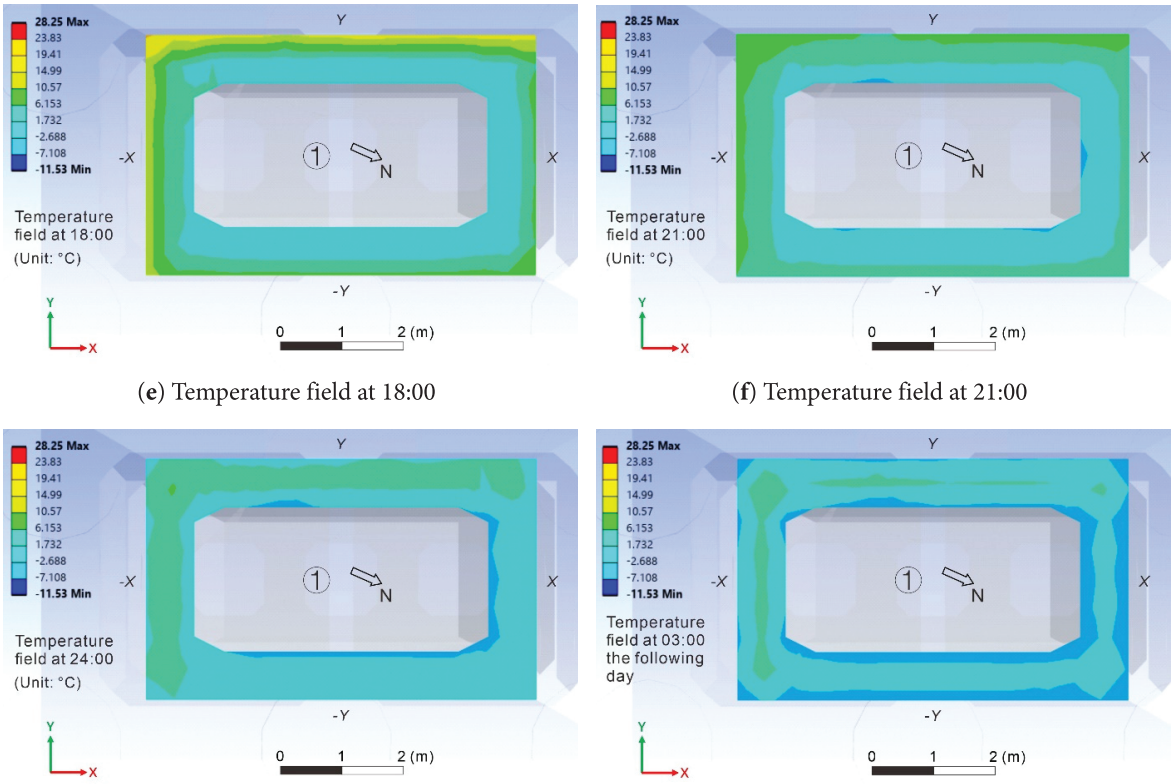

(**e**) Temperature field at 18:00

(**f**) Temperature field at 21:00

(**g**) Temperature field at 24:00

(**h**) Temperature field at 03:00 the following day

Figure 25: Temperature field cloud diagram of the horizontal cross-section of Sub-Pier ① at a height of 100 m on the main pier of the Zhaidi River Bridge under low temperature and low radiation condition in winter (Unit of temperatures in the figure is degree of Celsius): (a) Temperature field at 06:00; (b) Temperature field at 09:00; (c) Temperature field at 12:00; (d) Temperature field at 15:00; (e) Temperature field at 18:00; (f) Temperature field at 21:00; (g) Temperature field at 24:00; (h) Temperature field at 03:00 the following day

As shown in Fig. 25, during the winter solstice, the diurnal variation of the pier body temperature field corresponds well to the diurnal variation of the solar radiation intensity (Fig. 15b). At 06:00 in the morning (Fig. 25a), the temperature difference between the interior and exterior of the pier is not large, but there is still some uneven temperature distribution inside of the pier. As can be seen from Fig. 25a, even at 06:00 in the morning, the temperature of the concrete inside the pier near the Y and $-X$ side surfaces that receive solar radiation during the day is still about 10°C higher than that of the interior medium near the other two sides. At 9:00 (Fig. 25b), the $-X$ side surface begins to receive solar radiation, causing a slight rise in surface temperature. At 12:00 (Fig. 25c), the temperature of the $-X$ side surface increases significantly. As shown in Fig. 15b, the solar radiation intensity on the $-X$ side surface is near its peak at this time. At 15:00 (Fig. 25d), the sunlight begins to irradiate the Y side surface, causing the temperature on this side to rise; meanwhile, the $-X$ side surface is still at a relatively high temperature, so that the temperatures on these two side surfaces are nearly 20°C higher than those on the other two side surfaces. At 18:00 (Fig. 25e), the sun is about to set and the surface temperature of the pier begins to drop rapidly, and the heat conduction causes the temperature drop gradually transferring from the surface to the inside of the pier. At 21:00 (Fig. 25f) and 24:00 (Fig. 25g),

the temperature continues to drop. By 3:00 the next day (Fig. 25h), the temperature on the outer walls of the bridge pier is still dropping, especially the temperatures on the two sides (X side and $-Y$ side) that did not receive solar radiation during the day. It can be seen from the temperature field cloud diagrams at 21:00, 24:00, 3:00, and 06:00 that since the solar radiation is concentrated on the $-X$ side and Y side during the winter solstice (Fig. 15b), the temperature of the pier body concrete near these two sides is always higher than that near the other two sides.

4.2.3 Temperature-Induced Deformation Simulation Results of the High Bridge Pier

High Temperature and High Radiation condition in Summer

Corresponding to the temperature field of the Zhaidi River Bridge main pier under high temperature and high radiation condition in summer (Fig. 24), the cloud diagrams of the total displacement (three component synthetic displacement) of the temperature-induced deformation of the bridge pier at 06:00, 09:00, 12:00, 15:00, 18:00, 21:00, 24:00, and 03:00 the following day are as shown in Fig. 26. By comparison of the temperature-induced deformation displacement of the bridge pier in summer shown in Fig. 26 with the daily variation of solar radiation intensity on each side surface of the bridge pier shown in Fig. 15a and the temperature field variation depicted in Fig. 26, some corresponding relationships between the temperature-induced deformation and the solar radiation as well as the temperature field of the bridge pier under high temperature and high radiation condition in summer can be found.

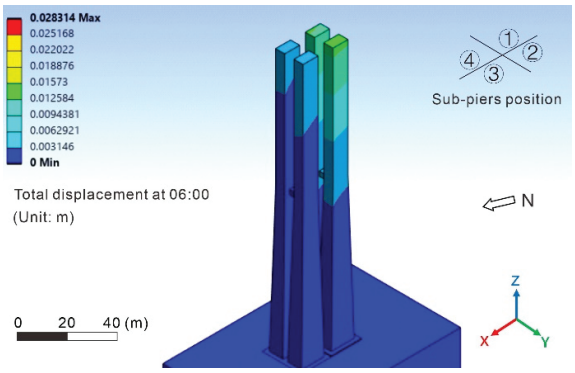

(**a**) Total displacement at 06:00

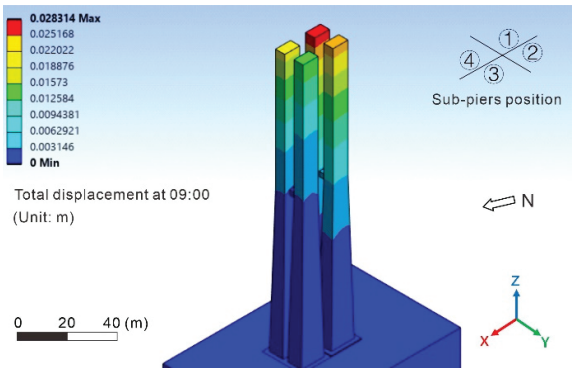

(**b**) Total displacement at 09:00

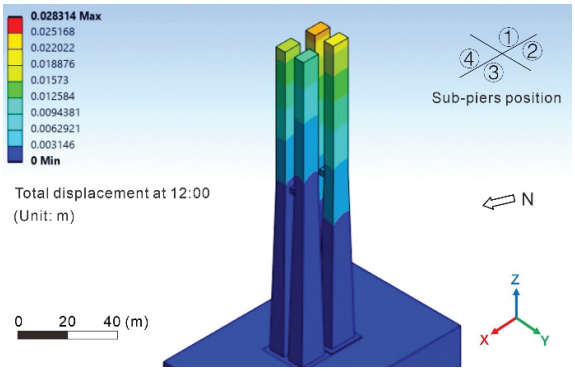

(**c**) Total displacement at 12:00

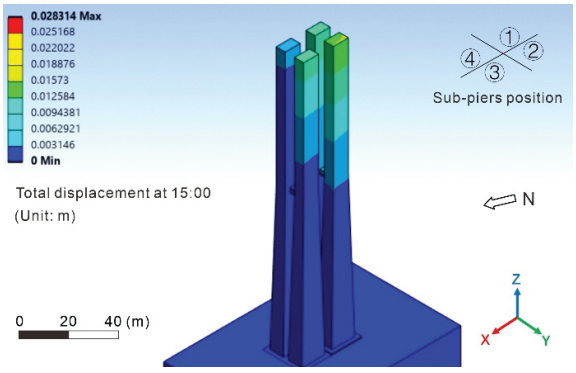

(**d**) Total displacement at 15:00

Figure 26: (Continued)

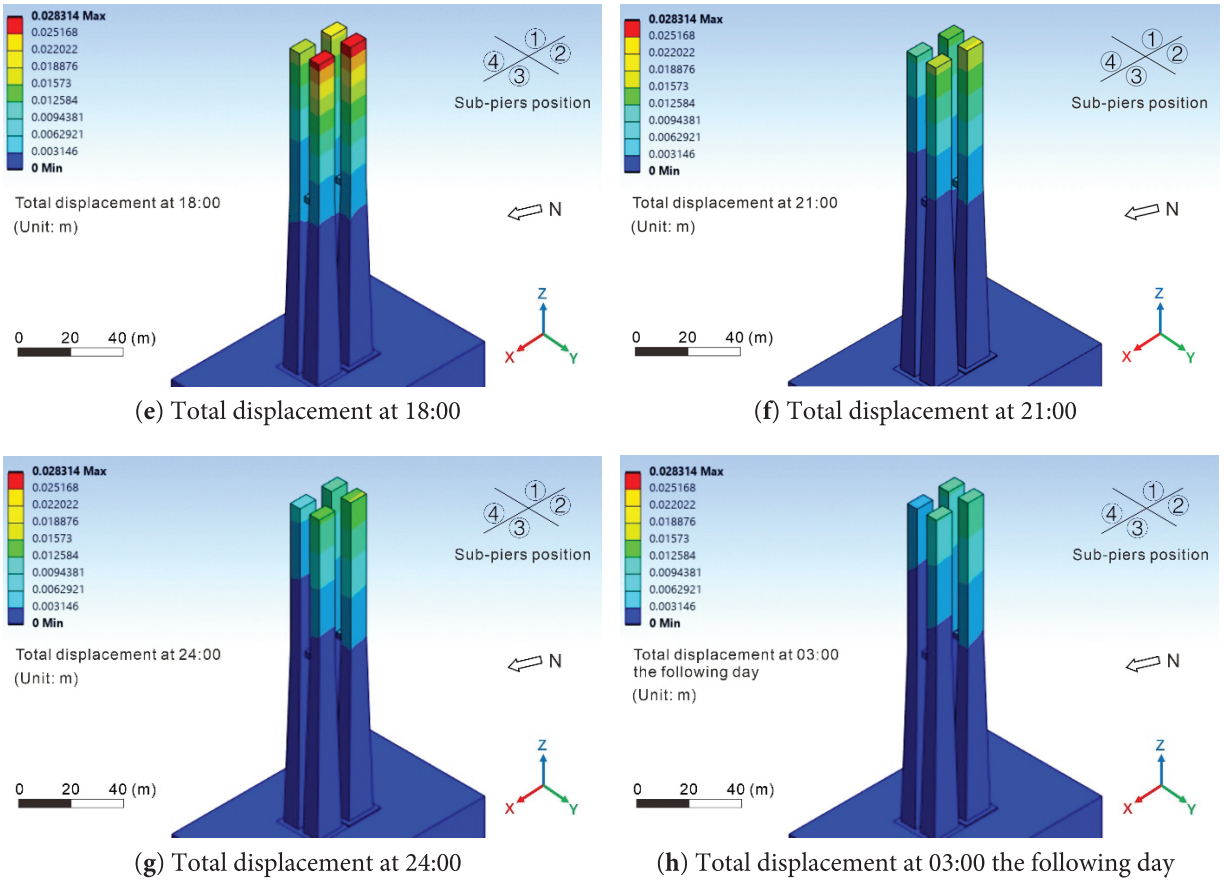

(**e**) Total displacement at 18:00

(**f**) Total displacement at 21:00

(**g**) Total displacement at 24:00

(**h**) Total displacement at 03:00 the following day

Figure 26: Total displacement field cloud diagrams of the main pier of the Zhaidihe Bridge due to temperature-induced deformation at different times a day under high temperature and high radiation condition in summer: (a) Total displacement at 06:00; (b) Total displacement at 09:00; (c) Total displacement at 12:00; (d) Total displacement at 15:00; (e) Total displacement at 18:00; (f) Total displacement at 21:00; (g) Total displacement at 24:00; (h) Total displacement at 03:00 the following day

At 06:00 in the morning, the sun has not yet risen, and the temperature field of the bridge pier remains in a balanced low temperature state formed at night. The temperature distribution within the pier is uniform (Fig. 24a), so the total displacement distribution of the temperature-induced deformation of the bridge pier is also relatively uniform (Fig. 26a), and the bridge pier will not deviate significantly from its vertical state. By 09:00 in the morning, the effect of solar radiation becomes apparent. The surface temperatures of the $-Y$ and $-X$ sides of the bridge pier rise due to the solar radiation, and uneven temperature distribution also appears in the cross-section of the bridge pier (Fig. 24b), so that the bridge pier displays noticeable uneven deformation (Fig. 26b). At 12:00, although the solar radiation intensities on the $-Y$ and $-X$ side surfaces drop rapidly, the deformation of the pier body near these two sides remains noticeable (Fig. 26c) due to the residual heat on these sides (Fig. 24c) and the rising air temperature (Fig. 16a). Around 15:00, the sunlight is incident almost vertically on the ground, so the intensity of solar radiation on the side of the bridge pier becomes very weak, and the temperature-induced deformation of the pier body also decreases accordingly (Fig. 26d).

By 18:00, the sun is close to the west, and the Y side surface of the bridge pier is subjected to stronger solar radiation, causing significant thermal expansion of the pier body near the Y side, and resulting in a large displacement of the pier pointing to the $-Y$ direction, the shady side of the pier (Fig. 26e). At 21:00, 24:00, and 03:00 the following day, as the sun sets, the temperature distribution across the bridge pier tends to be uniform (Fig. 24f–h), and the temperature-induced deformation of the bridge pier gradually decreases (recovery of temperature-induced deformation) until 03:00 the next day, when the horizontal deformation of the bridge pier becomes consistent (Fig. 26f–h). Under the condition of high temperature and high radiation in summer, the maximum total displacement of the pier in one day is 0.028 m, occurring on the bridge pier top at 19:00.

To further illustrate the total displacement variation of the pier body with time at different heights due to temperature-induced deformation, horizontal cross-sections of the bridge pier (including four sub-pier sections) are taken every 10 m in the height range of 0 to 110 m, and the maximum value of the total displacement of the temperature-induced deformation of each section over time within one day is extracted and shown in Fig. 27. As the height increases, the displacement of the bridge pier caused by temperature-induced deformation becomes more obvious. The temperature-induced deformation of the bridge pier above 60 m is significantly greater than that of the pier below 60 m. Additionally, the fluctuations in the maximum displacement of the horizontal cross-section at different heights of the pier body over time throughout the day closely follow the variation in solar radiation intensity over time, further indicating that **solar radiation is a major factor causing temperature-induced deformation of the pier**.

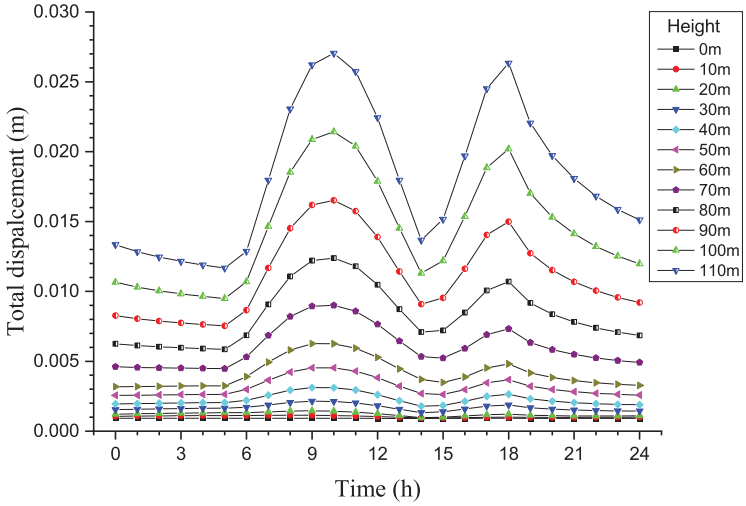

Figure 27: Daily variation curves of the maximum displacements due to temperature-induced deformation on different heights of the main pier of the Zhaidi River Bridge under high temperature and high radiation condition in summer

In order to analyze the variation of the total displacement of the pier with height at the same moment, the variation of the maximum temperature-induced displacement of the pier at different heights at 03:00, 06:00, 09:00, 12:00, 15:00, 18:00, 21:00, and 24:00 is shown in Fig. 28. It can be seen more intuitively from Fig. 28 that the pier displacement is larger when there is solar radiation than that when there is no solar radiation. Moreover, the displacement of the bridge pier increases with height, and the trend of displacement increasing with height becomes more and more obvious. Particularly around 60 m height of the bridge pier, the variation rate of displacement with height is significantly

different. The variation rate of the pier displacement with height above 60 m becomes significantly greater, and the cross-section where the pier body transitions from the varying cross-section height range to the constant cross-section height rangeis located exactly between the two heights of 60 m and 70 m (at height 62 m), which reflects **the control effect of the pier body geometry on the pier deformation**.

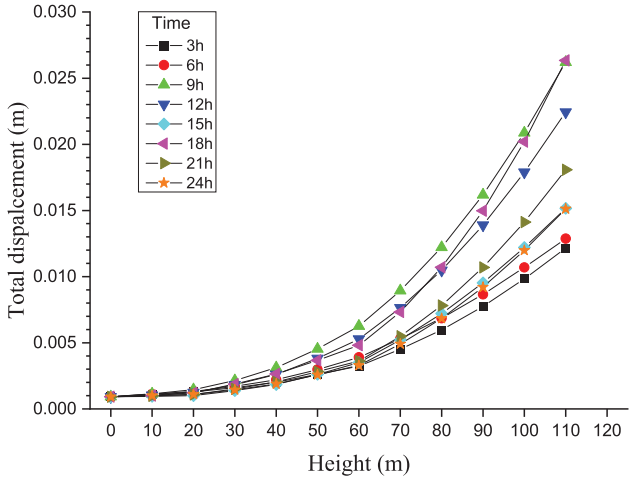

Figure 28: Variation of the pier maximum displacement with height of the main pier of the Zhaidihe Bridge at different times a day under high temperature and high radiation condition in summer

Low Temperature and Low Radiation condition in Winter

Corresponding to the temperature field of the main pier of the Zhaidi River Bridge under low temperature and low radiation condition in winter (Fig. 25), the total displacement (three-component synthesized displacement) of the temperature-induced deformation of the bridge pier at 06:00, 09:00, 12:00, 15:00, 18:00, 21:00, 24:00, and 03:00 the following day under the low temperature and low radiation condition in winter is shown in the displacement cloud diagrams in Fig. 29. By comparison of the total displacement of temperature-induced deformation shown in Fig. 29 with the daily variation of solar radiation intensity on each side surface of the pier in winter shown in Fig. 15b and the temperature field variation of the bridge pier in winter shown in Fig. 25, some corresponding relationships between the temperature-induced deformation and the solar radiation as well as the temperature field of the bridge pier under low temperature and low radiation condition in winter can be found.

As can be seen from Fig. 29a, at 06:00 in the morning, the sun has not yet risen, due to the uneven temperature distribution in the bridge pier concrete (Fig. 25a), the pier already has significant temperature-induced deformation without solar radiation thou. By 09:00 (Fig. 29b), noticeable temperature-induced deformation begins to appear in the pier body near to the $-X$ side. At 12:00 (Fig. 29c), 15:00 (Fig. 29d), and 18:00 (Fig. 29e), both the $-X$ and Y sides of the pier body show substantial temperature-induced deformation. At 21:00 (Fig. 29f), the temperature-induced deformation of the pier reduces, but by 03:00 the next day (Fig. 29h), significant deformation remains at the top of the pier. The maximum temperature-induced displacement occurs at the pier top at 19:00, with a value of 0.059 m.

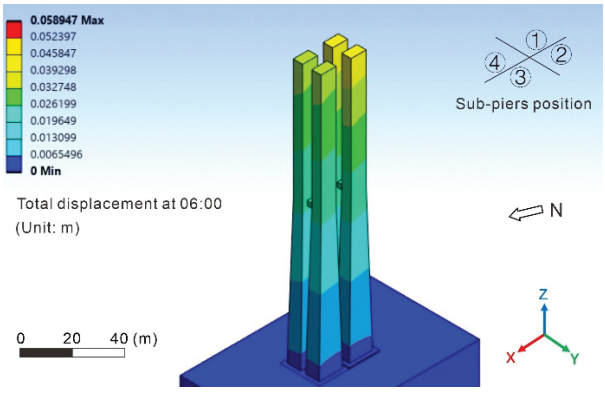

(**a**) Total displacement at 06:00

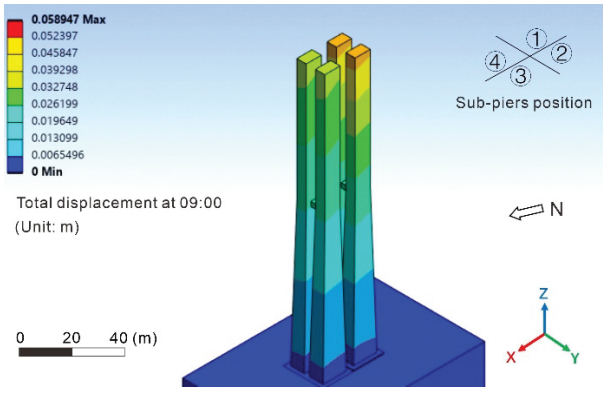

(**b**) Total displacement at 09:00

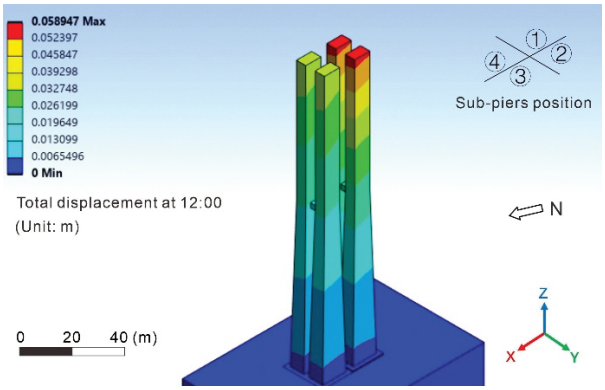

(**c**) Total displacement at 12:00

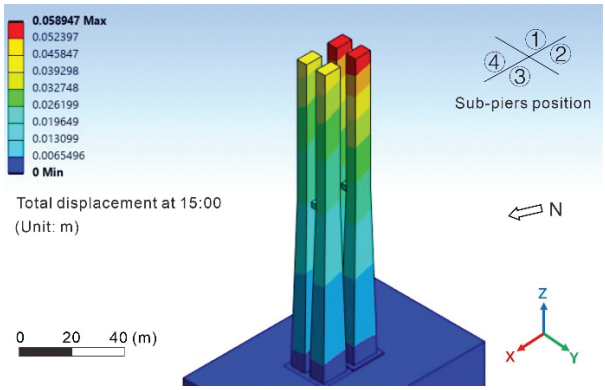

(**d**) Total displacement at 15:00

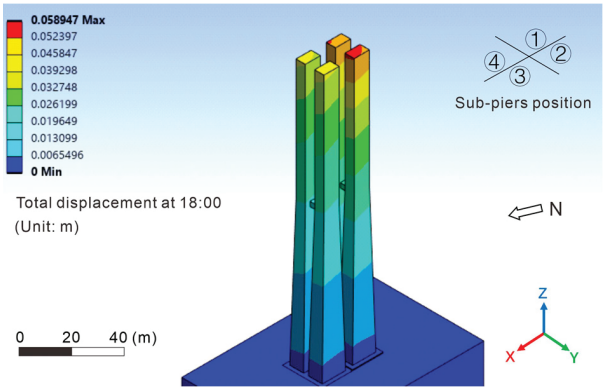

(**e**) Total displacement at 18:00

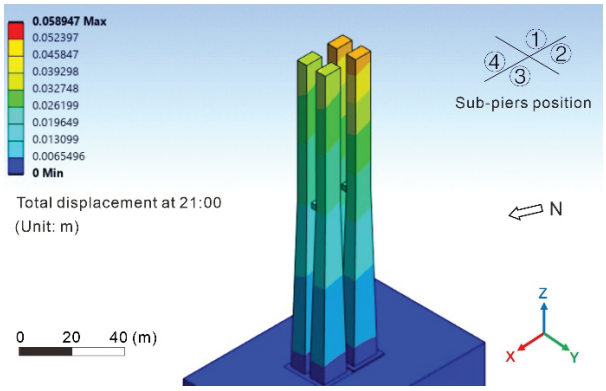

(**f**) Total displacement at 21:00

Figure 29: (Continued)

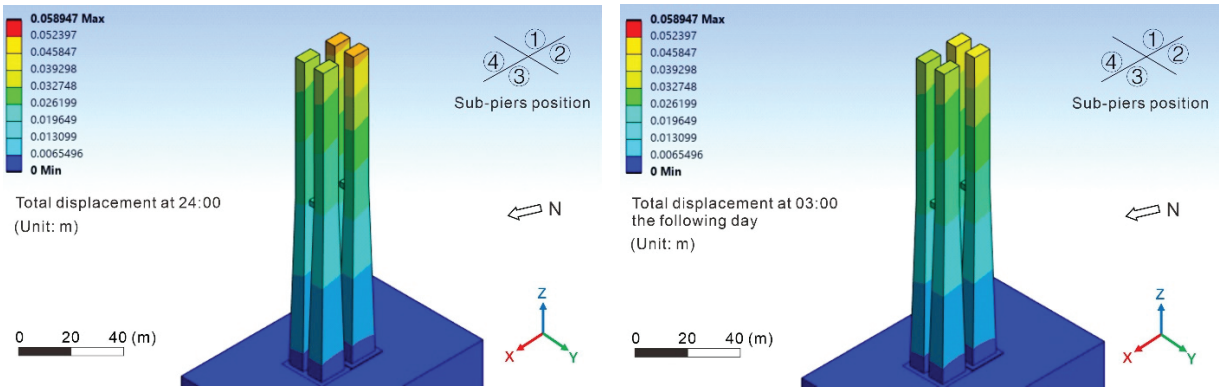

(**g**) Total displacement at 24:00 (**h**) Total displacement at 03:00 the following day

Figure 29: Total displacement field cloud diagrams of the main pier of the Zhaidi River Bridge due to temperature-induced deformation at different times a day under low temperature and low radiation condition in winter: (a) Total displacement at 06:00; (b) Total displacement at 09:00; (c) Total displacement at 12:00; (d) Total displacement at 15:00; (e) Total displacement at 18:00; (f) Total displacement at 21:00; (g) Total displacement at 24:00; (h) Total displacement at 03:00 the following day

To reveal the temperature-induced displacement variation of the pier body with time at different heights, horizontal cross-sections of the bridge pier are taken every 10 m in the height range from 0 to 110 m. The maximum total displacement of each horizontal cross-section over time within one day is extracted and plotted as shown in Fig. 30. From the comparison between Fig. 30 and Fig. 27, it can be seen that the temperature-induced deformation displacement of the pier under low temperature and low radiation condition in winter still increases with height, but this trend is not as pronounced as that under high temperature and high radiation condition in summer. Compared with the deformation of the bridge pier under high temperature and high radiation condition in summer, significant displacement is already observed at the height of 0 m, highlighting the temperature difference deformation effect caused by the difference in radiation intensity of solar radiation on different pier sides in winter. Therefore, during clear winter days with sustained sunlight, the bridge pier will experience greater temperature-induced deformation.

To analyze the variation of the overall pier displacement with height at the same moment, the maximum temperature-induced deformation displacement with height of the horizontal cross-section of the pier at 03:00, 06:00, 09:00, 12:00, 15:00, 18:00, 21:00, and 24:00 is shown in Fig. 31. It can be seen more intuitively from Fig. 31 that no matter what time, the pier displacement increases with height. Additionally, it can be seen from comparison of Fig. 27 with Fig. 30, and Fig. 28 with Fig. 31 that, unlike the temperature-induced deformation of the pier under high temperature and high radiation condition in summer, the temperature-induced displacement of the pier cross-section at different heights under low temperature and low radiation condition in winter has no obvious “mutation” over time. In the circumstance of low temperature and low radiation in winter, on the varying cross-section height range and the constant cross-section height range of the bridge pier above and below the horizontal cross-section corresponding to the height of 62 m, only occurs a slight difference in the variation rate of the temperature-induced deformation displacement with height (Figs. 30 and 31), but no very large variation amplitude in the temperature-induced displacement of the bridge pier with height as shown in Figs. 27 and 28.

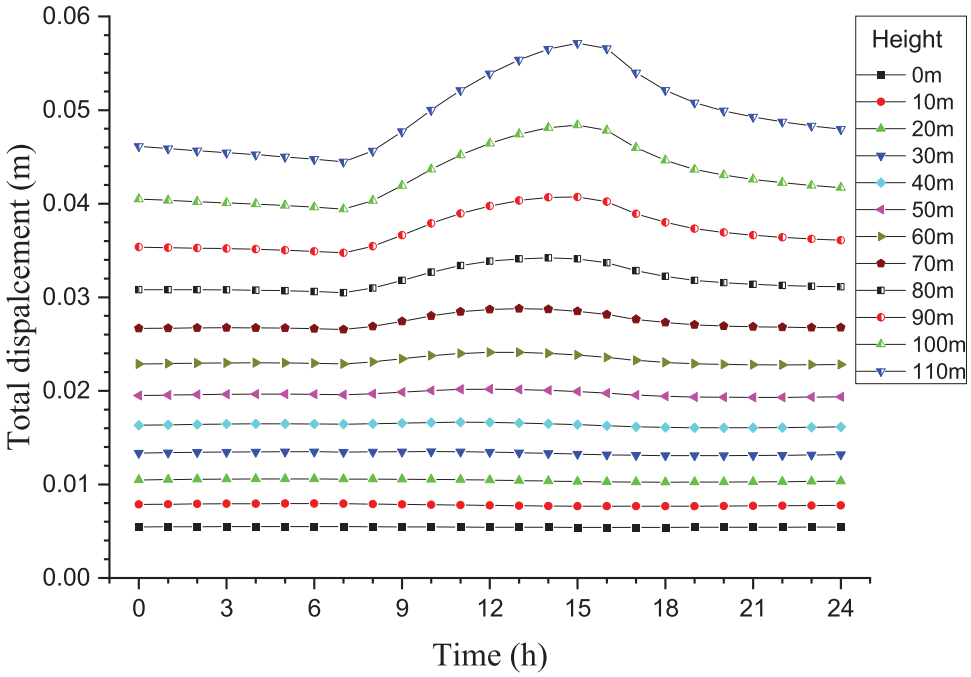

Figure 30: Daily variation curves of the maximum displacements due to temperature-induced deformation on different heights of the main pier of the Zhaidi River Bridge under low temperature and low radiation condition in winter

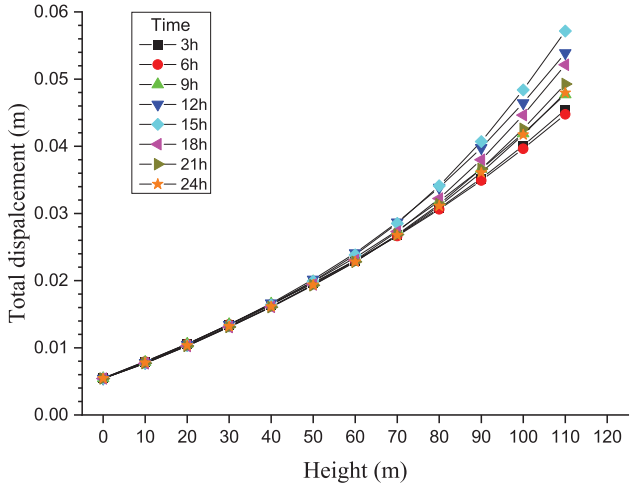

Figure 31: Variation of the maximum pier displacement with height of the main pier of the Zhaidi River Bridge at different times a day under low temperature and low radiation condition in winter

By comparison Figs. 26–28 (bridge pier temperature-induced deformation in summer) and Figs. 29–31 (bridge pier temperature-induced deformation in winter), it can be seen that **the temperature-induced deformation displacement of the pier body under low temperature and low radiation condition in winter is larger than that under high temperature and high radiation condition in summer**. The main reason is that in summer, each side of the bridge pier has almost equal opportunities to receive

solar radiation; while in winter, there are significant differences in the intensity of solar radiation received by different side surfaces of the bridge pier. As shown in Fig. 15, at the summer solstice, the solar elevation angle is large, and every side of the bridge pier has opportunity to receive solar radiation. Therefore, the overall heating of the bridge pier is relatively uniform throughout the day. Till the early morning of the next day, the temperature distribution inside and outside the bridge pier is still centrally symmetrical (Fig. 24h). However, the solar elevation angle is smaller during the winter solstice, and solar radiation is concentrated on the $-X$ and Y sides of the bridge pier. As a result, the temperature of these two sides is still higher than that of other sides till the early morning of the next day (Fig. 25h), and the bridge pier maintains an uneven temperature distribution for a long period of time. The fundamental reason for the temperature-induced deformation displacement of the bridge pier is the temperature difference between different sides. Although the overall temperature of the bridge pier in summer is higher than that in winter, the temperature difference between different sides of the bridge pier in summer is much smaller than that between different sides of the bridge pier in winter. Therefore, the temperature-induced deformation displacement of the bridge pier in summer is smaller than that of the bridge pier in winter.

4.3 Numerical Simulation Analysis of the Influence of Coupling Actioin of Wind Force and Temperature Variation on the Deformation of the High Bridge Pier

In natural environments, bridge piers are often simultaneously affected by wind forces and temperature variations. The simultaneous existence of wind force and temperature variation will produce two effects: one is the heat dissipation effect of wind, and the other is the superposition effect of wind-induced deformation and temperature-induced deformation.

On one hand, the air flow caused by wind blowing will accelerate the diffusion of heat from the sunny side of the bridge pier into the surrounding air, reducing the temperature difference between different sides of the pier, thereby reducing the temperature-induced deformation of the pier. To understand the heat dissipation effect of wind, the convective heat transfer coefficient values corresponding to different intensity levels of wind (i.e., different wind speeds) are obtained using Eq. (7), and these values are applied to the numerical simulation of the temperature-induced deformation of the bridge pier (without wind load) in the environment of high temperature and high radiation in summer and the environment of low temperature and low radiation in winter. The simulation result of the heat dissipation effect of the wind of different intensity levels (wind scales) on the temperature-induced deformation of the bridge pier is shown in Fig. 32. As shown in Fig. 32, whether it is under high temperature and high radiation condition in summer or low temperature and low radiation condition in winter, the temperature-induced deformation of the pier top decreases significantly with the increase of wind force level (this is a reflection of the heat dissipation effect of wind), and the temperature-induced deformation difference between different wind force levels also decreases significantly with the increase of wind force level (this shows that the difference between the heat dissipation effects of different wind force levels tends to decrease with the increase of wind force level). Especially, there is a relatively huge difference between the heat dissipation effects of wind (Wind scale > 0) and no wind (Wind scale $= 0$), but the difference between heat dissipation effects of different wind intensity levels is very small if there is wind. From the comparison of the daily variation curves of temperature-induced deformation displacement corresponding to different wind scales shown in Fig. 32, it can be seen that the time when the temperature-induced deformation is most significant is also the time when the heat dissipation effect is most obvious (manifested as the temperature-induced deformation difference corresponding to different wind scales at the same time is the largest, around 10 am in summer and around 16 pm in winter). In addition, it can be seen from

Fig. 32 that regardless of whether the heat dissipation effect of wind exists or not (with or without wind), the temperature-induced deformation of the pier in winter is all significantly larger than the temperature-induced deformation in summer.

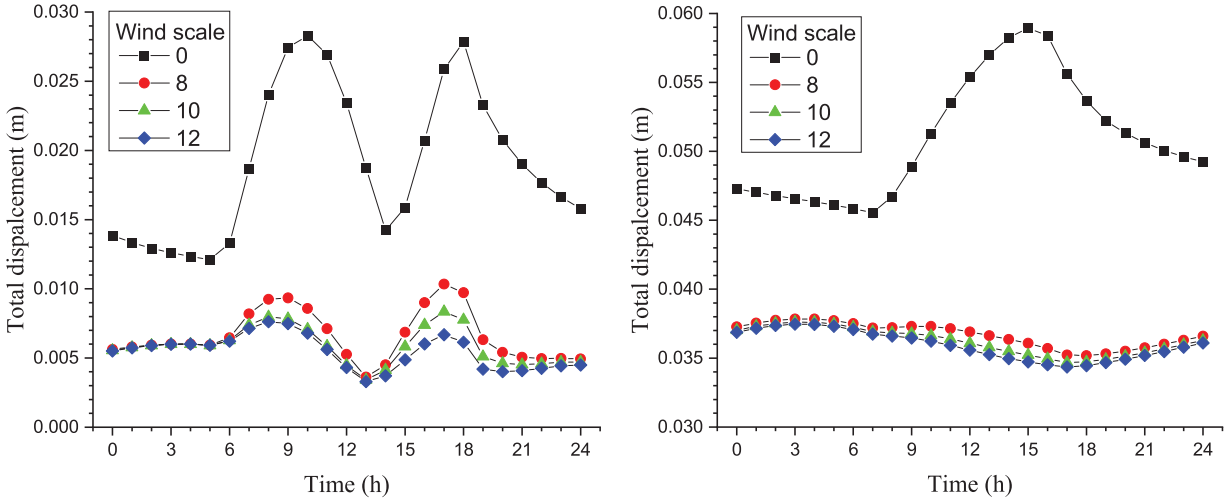

(**a**) High temperature and high radiation condition in summer

(**b**) Low temperature and low radiation condition in winter

Figure 32: Comparison of the influence of heat dissipation effect of wind of different wind scales on the daily variation of the maximum temperature-induced displacement of the pier top in summer (a) and in winter (b)

On the other hand, high-intensity wind forces cause the bridge pier to tilt to the downwind direction, which is much larger than the temperature-induced deformation. The temperature-induced deformation caused by solar radiation causes the pier to tilt toward the shady side. The inclination deformation of the bridge pier caused by the wind with different wind directions (for instance, south wind, S-N; north wind, N-S) and wind speeds (Wind scale 8, 10, and 12), and the temperature-induced deformation with a relatively fixed inclination direction caused by solar radiation will produce either a constructive (strengthening) or destructive (weakening) superposition effect of the pier deformation. Fig. 33 shows the comparison of superposition result (the maximum displacement the pier top) caused by the simultaneous action of the wind force of different intensity levels and different directions and the temperature variation under high temperature and high radiation condition in summer and low temperature and low radiation condition in winter. Two characteristics of the superposition effect of wind-induced deformatin and temperature-induced deformation of the bridge pier can be easily found from Fig. 33: 1) Whether under high temperature and high radiation condition in summer or under low temperature and low radiation condition in winter, the influence of wind force on the deformation of the bridge pier is far greater than that of temperature variation, that is, wind force is always the dominant factor affecting the deformation of the bridge pier after construction; 2) In winter when the solar radiation has a greater impact on the deformation of the bridge pier, the impact of wind direction on the deformation of the bridge pier is more significant. As shown in Fig. 33b, the wind-induced pier deformation caused by the south wind (S-N) and the temperature-induced pier deformation are constructively superimposed, whereas causes the wind-induced pier deformation caused by the north wind (N-S) and the temperature-induced pier deformation are destructively superimposed, therefore, the superimposed pier deformation caused by the coupling of the south wind and the temperature

variation is greater than that caused by the north wind and the temperature variation. Such kind of constructive and destructive superposition effect is not obvious in the daily variation curves of the pier deformation caused by the wind of different wind scales and the temperature variation under high temperature and high radiation conditions in summer shown in Fig. 33a.

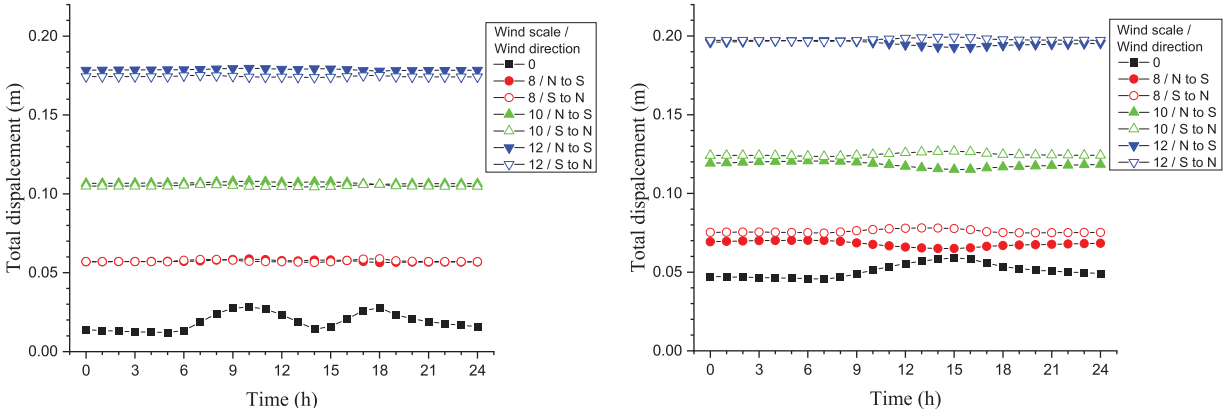

(**a**) High temperature and high radiation condition in summer

(**b**) Low temperature and low radiation condition in winter

Figure 33: Comparison of superposition results of temperature-induced deformation and wind-induced deformation at pier top caused by different wind scales and different wind directions: (a) High temperature and high radiation condition in summer; (b) Low temperature and low radiation condition in winter

5 Conclusions

This paper focuses on the influence of two natural loads, wind force and temperature variation, on the deformation of the high bridge pier after construction, and sorts out and explains the physical and mechanical principles regarding the influence of wind force, temperature variation and the coupling action of these two natural loads on the deformation of the bridge pier. Numerical simulations of the deformation of the Zhaidi River High Bridge Pier after construction caused by the action of wind force and temperature variation as well as the coupling of these two natural loads under two typical climate conditions, high temperature and high radiation condition in summer, low temperature and low radiation condition in winter, are carried out with the ANSYS finite element software Workbench Simulation Platform, and the influence of three key environmental factors: wind speed, ambient temperature, and solar radiation on the deformation of the high bridge pier is analyzed. Through the above research work and comprehensive analyses, the following understandings, and conclusions are obtained:

1. The direction of wind-induced deformation displacement of the bridge pier is the same as the wind direction. The value of wind-induced displacement gradually increases with the cross-section height of the pier, and the larger the height, the more obvious the trend of the increase in the pier displacement. The maximum displacement occurs at the top of the pier. The maximum values (the displacement at the pier top) of wind-induced displacement of the Zhaidi River High Bridge Pier caused by wind forces of scale 8, 10 (design basic wind), and 12 are 0.058 m, 0.110 m, and 0.185 m, respectively.

2. The daily variation in the temperature field and temperature-induced deformation displacement of the bridge pier are basically consistent with the daily variation of solar radiation intensity. The temperature rise area inside the pier is on the side of the sunlight, and the direction of the temperature-induced deformation displacement points to the shade side of the pier, indicating that the influence of solar radiation on the temperature distribution and temperature-induced deformation of the pier is far greater than that of ambient air temperature variation.
3. Temperature-induced deformation displacement of the bridge pier also gradually increases with the cross-section height of the pier, and the maximum temperature-induced deformation displacement occurs at the top of the pier. The maximum total temperature-induced deformation displacement of the pier under high temperature and high radiation conditions in summer is 0.028 m, while the maximum total temperature-induced displacement of the pier under low temperature and low radiation conditions in winter is 0.059 m. The temperature-induced deformation of the pier under lower temperature and lower solar radiation in winter is greater than that under high temperature and high radiation conditions in summer.
4. The variation amplitude of the temperature-induced deformation displacement with height of the upper segment of the bridge pier, whose cross-section keeps constant, is significantly larger than that of the lower segment of the bridge pier, whose cross-section is varying (shrinking) with height. This suggests that the pier structure has a significant control effect on the temperature-induced deformation of the pier.
5. Whether it is under high temperatures and high radiation in summer or under low temperatures and low radiation in winter, the impact of wind force on the deformation of the bridge pier is far greater than the impact of temperature variation on the deformation of the bridge pier.
6. The simultaneous existence of wind force and temperature variation will produce two main effects: the heat dissipation effect of wind and the superposition effect of wind-induced deformation and temperature-induced deformation. Heat Dissipation Effect: Regardless of whether it is thigh temperature and high radiation in summer, or low temperature and low radiation in winter, the temperature-induced deformation of the bridge pier will be significantly reduced due to the action of wind, and the more significant the temperature-induced deformation, the more obvious the heat dissipation effect of wind. Especially, there is a huge difference between the heat dissipation effects of wind (Wind scale > 0) and no wind (Wind scale < 0), however, the difference between heat dissipation effects of different wind intensity levels is very small if there is wind. Superposition effect of wind-induced deformation and temperature-induced deformations: The superposition of the downwind tilt deformation of the bridge pier caused by the wind of different directions and the temperature-induced deformation with a relatively fixed tilt direction (towards the shaded side) caused by solar radiation will produce a constructive (strengthening) or destructive (weakening) superposition effect of the pier deformation. In the northern hemisphere, the superposition of the wind-induced deformation caused by the south wind (S-N) and the temperature-induced deformation will make the deformation of the bridge pier enhanced (constructive superposition), while the superposition of the wind-induced deformation caused by the north wind (N-S) and the temperature-induced deformation will make the deformation of the bridge pier reduced (destructive superposition). The wind direction effect of the superposition of wind-induced deformation and temperature-induced deformation of the bridge pier more significant.

Based on the research in this paper, several suggestions that are meaningful for engineering practice are put forward:

1. The simulation results in this paper show that the variable cross-section design below the height 62 m of the Zhaidi River Bridge main pier 112.6 m tall does reduce the impact effect of wind load on thin-walled high bridge piers indeed, which is of reference value for the design of similar projects.
2. The superposition and coupling effects of wind action and temperature variation (wind heat dissipation, and the superposition of wind-induced and temperature-induced deformation) significantly impact bridge pier deformation. Numerical simulations (such as ANSYS finite element analysis) should be used during design to comprehensively evaluate the interactions of environmental factors such as wind direction, wind speed, and ambient temperature to ensure the safety and stability of bridge piers in extreme environments.
3. This study found that when the solar elevation angle is small, for instance, in high-latitude areas, the intensity of solar radiation received by different sides of the bridge pier varies greatly. Even when there is no solar radiation at night, the temperature inside the pier still shows an uneven distribution, thereby increasing the temperature-induced deformation displacement of the pier. On the contrary, in low-latitude areas, all sides of the bridge pier may have the opportunity to receive solar radiation, thus the temperature difference between the sides of the bridge pier is small, so the temperature-induced deformation displacement of the bridge pier is also relatively small. Therefore, more attention should be paid to the temperature difference deformation of bridge piers in high-latitude areas. The solar elevation angle is larger in summer, and the difference in solar radiation intensity on different sides of the bridge pier is relatively small. Therefore, bridge construction should be carried out in the summer as a priority.

Acknowledgement: The authors are deeply grateful to China Railway 24th Bureau Group Co., Ltd. for generously providing valuable data and design drawings, which laid a solid foundation for this research.

Funding Statement: Supported by China Railway 24th Bureau Group Co., Ltd.

Author Contributions: Conceptualization, Jinzhong Sun and Mengnan Tian; methodology, Jinzhong Sun and Mengnan Tian; software, Mengnan Tian and Xiang Chen; formal analysis, Mengnan Tian; data curation, Mengnan Tian; writing—original draft preparation, Mengnan Tian; writing—review and editing, Mengnan Tian, Jinzhong Sun and Feng Xiong; supervision, Jinzhong Sun; project administration, Jinzhong Sun. All authors reviewed the results and approved the final version of the manuscript.

Availability of Data and Materials: Not applicable.

Ethics Approval: Not applicable.

Conflicts of Interest: The authors declare no conflicts of interest to report regarding the present study.

References

1. Bleich F, Teller LW. Structural damping in suspension bridges. Trans Am Soc Civ Eng. 1952;117(1):165–95. doi:10.1061/TACEAT.0006638.

2. Tvrda K. Solution of a high bridge pillar under wind effects taking into account the real properties of reinforced concrete. MATEC Web Conf. 2020;313:00008. doi:10.1051/matecconf/202031300008.
3. Han Y, Chen ZQ, Hua XG, Feng ZQ, Xu G. Wind loads and effects on rigid frame bridges with twin-legged high piers at erection stages. Adv Struct Eng. 2017;20(10):1586–98. doi:10.1177/1369433216684350.
4. Wu W, Zhao C, Wu Y. Analysis of displacement method to determine the stability of pier under weight and wind loads. Highw Eng. 2014;39(2):135–8. (In Chinese).
5. Tadeu A, Marques da Silva F, Ramezani B, Romero A, Škerget L, Bandeira F. Experimental and numerical evaluation of the wind load on the 516 Arouca pedestrian suspension bridge. J Wind Eng Ind Aerodyn. 2022;220(6):104837. doi:10.1016/j.jweia.2021.104837.
6. Dai G, Tang Y, Liu Y. Numerical analysis of solar radiation temperature field of rounded end hollow tall pier of high-speed railway bridge. Bridge Constr. 2016;46(6):67–72. (In Chinese).
7. Chen S, Wu W, Yun J, Mao S, Yu Y. Prediction of uniform temperature effect on rectangular hollow concrete pier based on measured temperature data. Sci Rep. 2024;14(1):18803. doi:10.1038/s41598-024-69545-7.
8. Li J, Lu W, Gu H, Wang J. Study on temperature stress and temperature deformation of rectangular hollow thin wall high pier of high-speed railway bridge. In: Zhou Y, Li L, editors. 2020 International Conference on Intelligent Transportation, Big Data & Smart City (ICITBS); 2020 Jan 11–12; Vientiane, Laos. Washington, DC, USA: IEEE Computer Society; 2020. p. 387–93. doi:10.1109/ICITBS49701.2020.00084.
9. An L, Li D, Yuan P, Chen P. An analytical algorithm for determining optimal thin-walled hollow pier configuration with sunlight temperature differences. Buildings. 2023;13(5):1208. doi:10.3390/buildings13051208.
10. Sheng XW, Xiao SM, Zheng WQ, Sun HZ, Yang Y, Ma KL. Experimental and finite element investigations on hydration heat and early cracks in massive concrete piers. Case Stud Constr Mater. 2023;18(1):e01926. doi:10.1016/j.cscm.2023.e01926.
11. Do TA, Hoang TT, Bui-Tien T, Hoang HV, Do TD, Nguyen PA. Evaluation of heat of hydration, temperature evolution and thermal cracking risk in high-strength concrete at early ages. Case Stud Therm Eng. 2020;21(1):100658. doi:10.1016/j.csite.2020.100658.
12. Jin LJ, Fu JS, Liang JW, Liu Y. Dynamic response analysis of a long-span bridge with thin-walled high piers in valley terrain under combined wind and seismic effects. Thin-Walled Struct. 2025;212(4):113207. doi:10.1016/j.tws.2025.113207.
13. Yuan WK, Xie BC, Zhou WZ, Yin ZX, Wang ZW, Ding T. Seismic performance analysis of wind and rain bridge structures and design of a seismic vibration damping program using rubber isolators. Structures. 2025;79(1):109474. doi:10.1016/j.istruc.2025.109474.
14. Wu RE, Yang Q, Wang J, Li L, Ge DF, Guo SM, et al. Dynamic interaction analysis of long-span bridges under stochastic traffic and wind loads. Appl Sci. 2025;15(13):7577. doi:10.3390/app15137577.
15. Guo C, Zhang B, Guo H, Cui SG, Zhu B. Vehicle-bridge dynamic response analysis under copula-coupled wind and wave actions. Ocean Eng. 2023;285(6):115444. doi:10.1016/j.oceaneng.2023.115444.
16. Zhang J, Yang X, Dang X. Research on combination of seismic and temperature action effects of multi-span long continuous girder. In: Zhou Y, Li L, editors. 2020 International Conference on Intelligent Transportation, Big Data & Smart City (ICITBS); 2020 Jan 11–12; Vientiane, Laos. Washington, DC, USA: IEEE Computer Society; 2020. p. 327–31. doi:10.1109/ICITBS49701.2020.00074.
17. Mi SX, Wang YQ, Li L, Liao LJ, Huo XJ, Su W. Generalized algorithm for horizontal thermal displacement at the pier top of a railway simple-supported girder bridge. Structures. 2023;47(1):725–34. doi:10.1016/j.istruc.2022.11.062.
18. Zhang C, Shao J, Song L. Construction drawing design documents for the second section (K5+550~K11+085) of the Chenbeitun to Meihuibao segment (Yunnan Province) of the Zhenxiong to Hezhang Expressway. Beijing, China: CCCC Highway Consultants Co., Ltd; 2018. (In Chinese).

19. GB 18306-2015. Seismic ground motion parameter zonation map of China. Beijing, China: General Administration of Quality Supervision, Inspection and Quarantine of the People' s Republic of China & Standardization Administration of China. (In Chinese).
20. JTGD 60-2004. General specifications for design of highway bridges and culverts. Beijing, China: Ministry of Transport of the People' s Republic of China. (In Chinese).
21. GB 50010-2010. Code for design of concrete structures. Beijing, China: Ministry of Housing and Urban-Rural Development of the People' s Republic of China. (In Chinese).
22. JTG 3362-2018. Specifications for design of highway reinforced concrete and prestressed concrete bridges and culverts. Beijing, China: Ministry of Transport of the People' s Republic of China. (In Chinese).
23. JTG/T 3650-2020. Technical specification for construction of highway bridges and culverts. Beijing, China: Ministry of Transport of the People' s Republic of China. (In Chinese).
24. GB/T. Standard for design of concrete structure durability. Beijing, China: Ministry of Housing and Urban-Rural Development of the People' s Republic of China. (In Chinese).
25. Lin JH, Briseghella B, Xue JQ, Huang FY, Chen BC. Influence of material thermal parameters on temperature distribution on cross-section of concrete box girder. J Guangxi Univ Nat Sci Ed. 2020;45(1):53–60. (In Chinese).
26. Obinna U. Coefficient of thermal expansion of concrete [Internet]. Awka, Nigeria: Structville; 2020 [cited 2025 Jul 20]. Available from: https://structville.com/2020/04/coefficient-of-thermal-expansion-of-concrete.html.
27. EurocodeApplied. Table of concrete design properties [Internet]. [cited 2025 Jul 20]. Available from: https://eurocodeapplied.com/design/en1992/concrete-design-properties.
28. GB 50009-2012. Load code for the design of building structures. Beijing, China: Ministry of Housing and Urban-Rural Development of the People' s Republic of China. (In Chinese).
29. Wikipedia. Beaufort scale [Internet]. San Francisco, CA, USA: Wikimedia Foundation; 2025 [cited 2025 July 20]. Available from: https://en.wikipedia.org/wiki/Beaufort_scale.
30. Wikipedia. Thermal radiation [Internet]. San Francisco, CA, USA: Wikimedia Foundation; 2025 [cited 2025 July 20]. Available from: https://en.wikipedia.org/wiki/Thermal_radiation.
31. Wikipedia. Stefan–Boltzmann law [Internet]. San Francisco, CA, USA: Wikimedia Foundation; 2024 [cited 2025 May 10]. Available from: https://en.wikipedia.org/wiki/Stefan%E2%80%93Boltzmann_law.
32. Peng S. Studies on theory of solar radiation thermal effects on concrete bridges with application [Dissertation]. Chengdu, China: Southwest Jiaotong University; 2007. (In Chinese).
33. Dilger WH, Amin G, Chan M, Tan J. Temperature stress in composite box girder bridges. J Struct Eng ASCE. 1983;109(6):1460–79. doi:10.1061/(asce)0733-9445(1983)109:6(1460).
34. Barber E. Calculation of maximum pavement temperatures from weather reports. Washington, DC, USA: Highway Research Board; 1957.
35. Elbadry M, Ghali A. Temperature variations in concrete bridges. J Struct Eng ASCE. 1983;109(10):2355–74. doi:10.1061/(asce)0733-9445(1983)109:10(2355).
36. Tianqi. Temperature of Zhaotong, Yunnan [Internet]. Chongqing, China: Tianqiwang; 2021 [cited 2025 May 11]. Available from: https://www.tianqi.com/qiwen/city_zhaotong/.
37. BYJU' S. Fourier' s law [Internet]. Bengaluru, India: BYJU' S; 2025 [cited 2025 Jul 24]. Available from: https://byjus.com/physics/fouriers-law/.
38. Wikipedia. Thermal conductivity and resistivity [Internet]. San Francisco, CA, USA: Wikimedia Foundation; 2025 [cited 2025 Jun 14]. Available from: https://en.wikipedia.org/wiki/Thermal_conductivity_and_resistivity.
39. Wikipedia. Heat equation [Internet]. San Francisco, CA, USA: Wikimedia Foundation; 2025 [cited 2025 Jun 15]. Available from: https://en.wikipedia.org/wiki/Heat_equation#Specific_examples.

40. Tianqi. Weather in Zhenxiong in December 2019 [Internet]. Chongqing, China: Tianqiwang; 2019 [cited 2025 Aug 29]. Available from: https://lishi.tianqi.com/zhenxiong/201912.html.
41. ANSYS. ANSYS documentation. Canonsburg, PA, USA: ANSYS, Inc.; 2017.